Die approbierte Originalversion dieser Diplom-/Masterarbeit ist an der Hauptbibliothek der Technischen Universität Wien aufgestellt (http://www.ub.tuwien.ac.at).

The approved original version of this diploma or master thesis is available at the main library of the Vienna University of Technology (http://www.ub.tuwien.ac.at/englweb/).

DIPLOMARBEIT

InGaAs / GaAsSb Resonant Tunneling Diodes

ausgeführt zum Zwecke der Erlangung des akademischen Grades eines
Diplom-Ingenieurs

unter der Leitung von

Univ.Prof.Dr. Gottfried Strasser
Institut für Festkörperelektronik
E362

eingereicht an der Technischen Universität Wien
Fakultät für Elektrotechnik

von

Michael Schwantzer, B.Sc.

Mat.Nr. 9826139
Maurichgasse 20/35
A-1220 Wien

Wien, im April 2011

Betreuer:
Dipl.Ing. Hermann Detz
Univ.Prof.Dr. Gottfried Strasser

Kurzfassung

Resonante Tunneldioden (RTDs) haben viele mögliche Anwendungsgebiete, etwa als ultraschnelle Schalter, als Oszillatoren zur Erzeugung von hohen Frequenzen bis zu 1 THz bei Raumtemperatur oder in der Forschung von quantenmechanischen Transporteffekten. Zur Herstellung von RTDs können eine Vielzahl an Materialien, wie III-V und II-VI Halbleiter, eingesetzt werden. In dieser Diplomarbeit wurden RTDs zur Analyse und Charakterisierung von Heterostrukturen für das aluminiumfreie $\mathrm{In}_x\mathrm{Ga}_{1-x}\mathrm{As}/\mathrm{GaAs}_x\mathrm{Sb}_{1-x}$ Materialsystem verwendet. Diese gitterangepassten Strukturen wurden durch Molekularstrahlepitaxie (MBE) auf InP Substrat gewachsen. Dieses Materialsystem verspricht eine Verbesserung der Eigenschaften von Halbleiterheterostrukturen wie dem Quantenkaskadenlaser, den Quantentopf-Infrarot-Photodetektoren oder auch von resonanten Tunneldioden. Das Herstellungsverfahren von 100µm x 100µm, 40µm x 40µm, 30µm x 30µm, 10µm x 10µm und 5µm x 5µm RTDs wurde optimiert, um bestmögliche Ergebnisse bei der Erzeugung von RTDs zu erzielen. Die hergestellten RTDs besitzen einen Quantentopf aus $\mathrm{In}_x\mathrm{Ga}_{1-x}\mathrm{As}$ der Breite von 7 nm, 10 nm, 13 nm und 20 nm und 9 nm dicke $\mathrm{GaAs}_x\mathrm{Sb}_{1-x}$ Barrieren auf beiden Seiten des Quantentopfes. Diese Variation der Dicke des Quantentopfes soll zu weiteren Erkenntnissen beitragen, ob es eine Verbindung zwischen den unterschiedlichen Dicken der Quantentöpfe und dem *Peak-to-Valley Ratio* (PVR), den symmetrischen Strom-Spannungs-Kennlinien (I-V Kennlinien) und magnetisch induzierten Effekten gibt. Diese Quantentransportmessungen unter magnetischen Feldern (Silvano de Sousa *et al.*) wurden an den im Rahmen dieser Arbeit hergestellten RTDs ausgeführt, dabei wurde das sogenannte *resonance peak splitting* Phänomen gefunden.

I-V Kennlinien wurden bei 300 K (Raumtemperatur), 78 K und 4.2 K untersucht und Resonanzen, die für den negativen differenziellen Widerstandsbereich (NDR) verantwortlich sind, wurden auch noch bei Raumtemperatur beobachtet. Der Einfluss der SiN Isolationsschicht auf das I-V Verhalten wurde untersucht und es zeigt sich, dass RTDs ohne diese Isolierungschicht größeres PVR aufweisen. Desweiteren erlaubt die Untersuchung von PVRs der einzelnen Proben unterschiedlicher Quantentopfdicke erste Rückschlüsse über einen möglichen Zusammenhang zwischen der Größe der RTD und ihrem PVR. Vergleiche von 40µm x 40µm, 10µm x 10µm und 5µm x 5µm RTDs zeigen, dass mit einer Reduktion der Größe der RTD der PVR aufgrund der geringer werdenden Wahrscheinlichkeit von Oberflächendefekten ansteigt.

Weiters wurde die Auswirkung von Interfacerauhigkeiten zwischen den $\mathrm{In}_x\mathrm{Ga}_{1-x}\mathrm{As}$ und $\mathrm{GaAs}_x\mathrm{Sb}_{1-x}$ Schichten untersucht. Diese Interfacerauhigkeit scheint eine wichtige Rolle für das Verhalten der I-V Kennlinie in symmetrischen Strukturen in Abhängigkeit der tatsächlichen Stromrichtung zu spielen, insbesonderes für dünne Quantentöpfe, da der Einfluss der Interfacerauhigkeit mit zunehmender Dicke des Quantentopfes abnimmt.

Abstract

Resonant tunneling diodes (RTDs) have a wide range of possible applications. They are used as ultra-fast switches, as research devices for quantum transport physics and even as high-frequency oscillators up to 1 THz at room-temperature. Furthermore, a vast variety of materials, such as III-IV and II-VI semiconductors, respectively material compounds can be used for fabrication. In this thesis, RTDs were used to analyse and characterise heterostructures in the aluminum free $\mathrm{In}_x\mathrm{Ga}_{1-x}\mathrm{As}/\mathrm{GaAs}_x\mathrm{Sb}_{1-x}$ material system. The structures were grown lattice-matched to InP substrates by molecular beam epitaxy. This material system promises improvements to the performance of semiconductor heterostructure devices like quantum cascade lasers, quantum-well infrared photodetectors or to the RTDs itself due to relatively small effective masses of electrons in both compounds. Fabrication recipes for 100µm x 100µm, 40µm x 40µm, 30µm x 30µm, 10µm x 10µm and 5µm x 5µm RTDs have been tested and improved to allow easy reprocessing and adjustment to for further research. The fabricated RTDs consist of different $\mathrm{In}_x\mathrm{Ga}_{1-x}\mathrm{As}$ quantum-well widths of 7 nm, 10 nm, 13 nm and 20 nm and 9 nm $\mathrm{GaAs}_x\mathrm{Sb}_{1-x}$ barriers on each side of the well. The variation of the well thickness was done to further investigate relations between *Peak-to-Valley Ratio* (PVR), I-V characteristics, and effects of magnetic fields. These transport measurements under magnetic fields (Silvano de Sousa *et al.*) were instigated by using the RTDs fabricated within this thesis. A resonance peak splitting phenomenon was found during these magnetic field experiments.

I-V curves have been measured at 300 K (room-temperature), 78 K, and at 4.2 K and resonances, resulting in negative differential resistance, have been seen up to 300 K. Influence of the SiN isolation on I-V behaviour has been investigated and has shown a higher PVR for RTDs without SiN isolation layers. Furthermore, the PVR of samples with different well widths allows the conclusion that there is a connection between the size of the RTD and its PVR. Comparison of 40µm x 40µm, 10µm x 10µm and 5µm x 5µm RTDs indicates, that the smaller the actual size of the RTD, the higher the PVR becomes due to the reduced influence of surface defects. Last, but not least, the importance of interface roughness between the $\mathrm{In}_x\mathrm{Ga}_{1-x}\mathrm{As}$ and $\mathrm{GaAs}_x\mathrm{Sb}_{1-x}$ layers for different variations of quantum-well thickness has been investigated and interface roughness was proven to play a vital role for I-V behaviour for different current directions in symmetric structures. This is especially important for thin wells, as the influence of the interface roughness decreases with increasing well thickness.

Contents

Contents 7

1 Introduction **9**

1.1 Thesis Outline . . . 10

2 Resonant Tunneling Diodes Physics **13**

2.1 $\mathrm{In}_x\mathrm{Ga}_{1-x}\mathrm{As}/\mathrm{GaAs}_x\mathrm{Sb}_{1-x}$ Material System . . . 13

2.1.1 Characteristics and Bandstructure of $\mathrm{In}_x\mathrm{Ga}_{1-x}\mathrm{As}$ . . . 14

2.1.2 Characteristics and Bandstructure of $\mathrm{GaAs}_x\mathrm{Sb}_{1-x}$ . . . 15

2.1.3 Characteristics of $\mathrm{In}_x\mathrm{Ga}_{1-x}\mathrm{As}/\mathrm{GaAs}_x\mathrm{Sb}_{1-x}$ . . . 17

2.2 Tunneling . . . 18

2.2.1 Tunneling in Single-Barrier Structures . . . 19

2.2.2 Tunneling in Double-Barrier Heterostructures . . . 26

2.3 Characteristics of Resonant Tunneling Diodes . . . 32

2.3.1 Ohmic Contacts . . . 32

2.3.2 Basic RTD Quantities . . . 34

3 Fabrication Technologies and Recipes **39**

3.1 Technology for *III-V* Semiconductor Device Fabrication . . . 39

3.1.1 Molecular Beam Epitaxy . . . 39

3.1.2 Plasma Enhanced Chemical Vapor Deposition . . . 41

3.1.3 Lithography . . . 42

3.1.4 Reactive Ion Etching . . . 44

3.1.5 Evaporation . . . 47

3.1.6 Sputtering . . . 48

3.2 Fabrication Recipes of Processed Resonant Tunneling Diodes . . . 51

3.2.1 Processing 1 - RTD size: 100µm x 100µm, 30µm x 30µm, 10µm x 10µm 52

3.2.2 Processing 2 - RTD size: 40µm x 40µm, 10µm x 10µm, 5µm x 5µm . 55

4 Characterisation of Resonant Tunneling Diodes **59**
4.1 Basic Quantities 59
4.1.1 Growth Sheet 59
4.1.2 Bandstructure 61
4.2 Current-Voltage Characteristics 64
4.3 Peak-to-Valley Ratio versus RTD size 71
4.4 Interface Induced Asymmetry Effect 73
4.5 Magnetic Effects on the In$_x$Ga$_{1-x}$As/GaAs$_x$Sb$_{1-x}$ Material System 76

5 Summary **79**

6 Outlook **81**

A Growth Sheets **83**

List of Figures **85**

List of Tables **89**

Bibliography **91**

Chapter 1

Introduction

The enormous progress in technology of crystalline growth, since molecular beam epitaxy (MBE) was firstly introduced in the 60s (for an overview see [1]) into the research of material science, allows a steady growing research field for novel semiconductor devices. These devices differ in their practical use for applications depending on size, fabrication process and most of all in the used material composition. Further development and research on deposition and growth technology lead to achieving more and more information about engineering complex material compositions, especially for III-V materials, with so far not researched characteristics and behaviour for a variety of applications. New materials bear the hope of improving already existing semiconductor devices in performance, speed or stability. Therefore, it is from the utmost interest to research these newly formed material systems as soon as the growth technology is ready to provide the necessary methods.

At the moment, state-of-the-art intersubband (ISB) devices, as the quantum-cascade laser (QCL) or quantum-well infrared detectors (QWIP), are realized in a variety of material systems. GaAs/$\mathrm{Al}_x\mathrm{Ga}_{1-x}\mathrm{As}$ is often used for QWIPs [2], while QCLs are frequently realized in $\mathrm{In}_{0.53}\mathrm{Ga}_{0.47}\mathrm{As}/\mathrm{In}_{0.52}\mathrm{Al}_{0.48}\mathrm{As}$ [3] as well as in GaAs/$\mathrm{Al}_x\mathrm{Ga}_{1-x}\mathrm{As}$ [4]. Furthermore, experiments with II-VI semiconductor combinations have been done to realize QCLs.[5], [6] All above mentioned III-V material systems have a noticeable aluminum content inside the barrier material. On one side, this allows a large conduction band offset (CBO), however on the other side is the disadvantage of higher electron mass. In particular, the higher electron mass inside the barriers due to the high aluminum percentage, leads to a rising dark current of QWIPs.[7] Furthermore, to rise QCLs efficiency, the effective masses should be as low as possible to ensure longer lifetimes of electrons in the upper laser levels.[8]

Last but not least, growing Al on GaAs surfaces during molecular beam epitaxy rises other problems, like increased surface roughness.[9] Due to this effects, efforts are made to use Al-free III-V material systems. One promising candidate, because of the low effective masses for electrons, is $\mathrm{In}_{0.53}\mathrm{Ga}_{0.47}\mathrm{As}/\mathrm{GaAs}_{0.51}\mathrm{Sb}_{0.49}$. Extensive research efforts are undertaken to further deepen the understanding of the behaviour of this material.[9]

As an example, performance enhancement of HEMTs and HBTs can be seen in Fig.1.1 as a result of switching material systems.

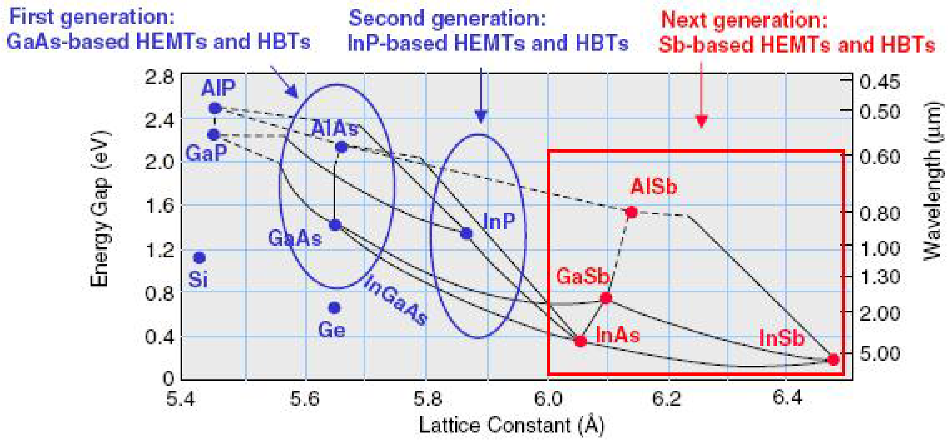

Figure 1.1: Lattice constants for a variety of materials.[10]

At the moment, one of the most widely used devices for semiconductor nano-structure testing, is the resonant tunneling diode (RTD). RTDs are used to gather information about behaviour and characteristic of new material systems and are based on resonant tunneling. Therefore, resonant tunneling diodes are best to be described as double-barrier heterostructure devices, featuring massive tunneling current at certain energy levels, leading to a negative differential resistance (NDR). Additionally, beside the importance of RTDs as a testing ground for optoelectronic intersubband applications (ISB), it is also commonly found in a variety of applications like multi-valued data storage or high-frequency oscillators.[11]

1.1 Thesis Outline

This diploma thesis contains four chapters which will be shortly introduced in the following. Chapter 1 functions as introduction to the topic of the diploma thesis as well as an explanation for the motivation for this topic. Furthermore, chapter 1 provides an outlook of what to expect in this work.

Chapter 2 is a theory chapter presenting the physics behind resonant tunneling diodes (RTD), starting by an excursus into the used material system $\mathrm{In}_x\mathrm{Ga}_{1-x}\mathrm{As}/\mathrm{GaAs}_x\mathrm{Sb}_{1-x}$ and selectively chosen parameters and important constants will be shown about the material system as well as the bandstructure of each material. Afterwards, based on the principle of motion in quantum-mechanics, this thesis gives a deeper insight into the the important transport effect of tunneling. By switching from classical physics to quantum mechanics, tunneling must be considered for particle motion behaviour. Starting by the effects of single-barrier tunneling, subsequently tunneling through double-barrier heterostructures is explained by expanding the given theory about single-barrier tunneling. This allows to characterise the function of RTDs. Furthermore, a more detailed explanation of ohmic contacts is given in this chapter, because of it's importance of neglecting parasitic contact effects, which occur on Schottky contacts. This is the pre-condition for exact measurements of RTD behaviour.

Chapter 3 firstly addresses the fabrication technologies for processing RTDs. This includes a more detail description of growing (Molecular Beam Epitaxy), deposition (for example Physical Enhanced Chemical Vapor Deposition), etching (Reactive Ion Etching) and pattering (Lithography) techniques. Then detailed recipes for both RTDs designs, used to fabricate all RTDs, which were processed during the practical work of this thesis, are listed.

Finally in chapter 4, all achieved results are presented. The results contain current-voltage characteristics (IV's), bandstructures and more. At the very end, a summary of the achieved results is given, where magnetic transport measurements were done by Silvano de Sousa, Jürgen Smoliner *et al.*, followed by short outlook of possible things to come.

Chapter 2

Resonant Tunneling Diodes Physics

In this chapter, a detailed introduction of the material system $\mathrm{In}_x\mathrm{Ga}_{1-x}\mathrm{As}/\mathrm{GaAs}_x\mathrm{Sb}_{1-x}$ will be given, including basic parameters like lattice constant or electron mass of each material as well as the bandstructures of $\mathrm{In}_x\mathrm{Ga}_{1-x}\mathrm{As}$ and $\mathrm{GaAs}_x\mathrm{Sb}_{1-x}$. Afterwards, the physics of resonant tunneling diodes will be presented in more detail to allow further understanding of upcoming results in chapter 4. This includes explaining the tunneling process for symmetric and asymmetric single-barrier heterostructures and based on this theory, expanding it to achieve knowledge about double-barrier heterostructures. As for single-barrier structures, double-barrier formalism for the symmetrical and the asymmetrical case will be shown. The results of double-barrier heterostructure tunneling is necessary to provide the knowledge to understand the later on presented basic properties of resonant tunneling diodes. At the end of this chapter RTDs characterisation is given for upcoming results for $\mathrm{In}_x\mathrm{Ga}_{1-x}\mathrm{As}/\mathrm{GaAs}_x\mathrm{Sb}_{1-x}$ RTDs in chapter 3 and chapter 4 as well as a short introduction to the necessity of ohmic contacts is shown. The theory in this chapter, especially about tunneling through single-barrier and double-barrier semiconductor structures, is mostly based on following books: *Transport in Nano-structures by David K. Ferry and Stephen M. Goodnick[12]* and *The Physics and Applications of Resonant Tunneling Diodes by Hiroshi Mizuta and Tomonori Tanoue.[11]*

2.1 $\mathrm{In}_x\mathrm{Ga}_{1-x}\mathrm{As}/\mathrm{GaAs}_x\mathrm{Sb}_{1-x}$ Material System

As shown in already published papers [13] and [14], promising results were achieved by using the relatively new material system $\mathrm{In}_x\mathrm{Ga}_{1-x}\mathrm{As}/\mathrm{GaAs}_x\mathrm{Sb}_{1-x}$ for Intersubband devices, especially for quantum cascade lasers in the THz-range. Therefore, the main part of this diploma thesis was to further deepen the knowledge about the characteristics and the behaviour of the material system $\mathrm{In}_x\mathrm{Ga}_{1-x}\mathrm{As}/\mathrm{GaAs}_x\mathrm{Sb}_{1-x}$. Resonant tunneling diodes are often used as a characterization tool for material behaviour as well as for high frequencies electronics.[11],[15],[16],[17] Therefore, RTDs were used for the testing studies and naturally all fabricated resonant tunneling diodes for this diploma thesis were based on $In_xGa_{1-x}As/$ $GaAs_xSb_{1-x}$. Precisely on superlattices of $In_{0.53}Ga_{0.47}As/GaAs_{0.51}Sb_{0.49}$ matched to an InP substrate. $GaAs_{0.51}Sb_{0.49}$ was used as barrier material while $In_{0.53}Ga_{0.47}As$ was used for the quantum well. The lattice constant of different semiconductor materials is shown in Fig.2.1. The material system was grown by molecular beam epitaxy inside the clean-room at the Center of Micro- and Nanostructures at the Vienna University of Technology.

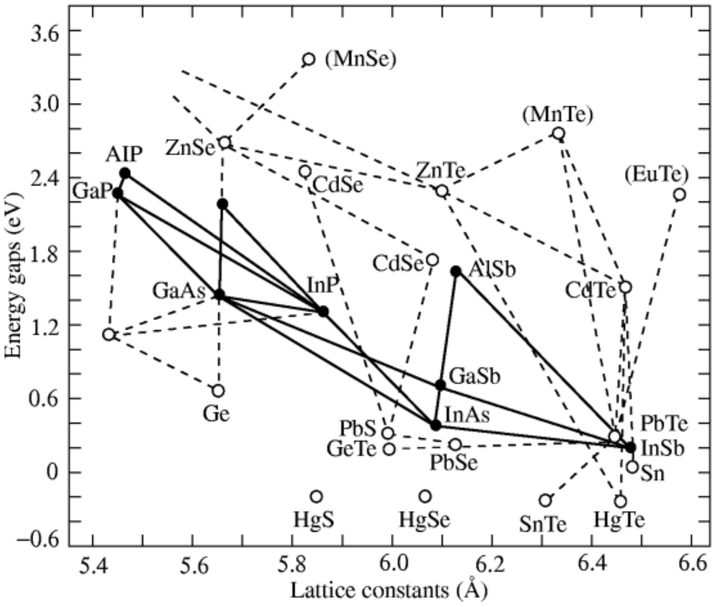

Figure 2.1: Lattice constants for a variety of materials.[18]

2.1.1 Characteristics and Bandstructure of $In_xGa_{1-x}As$

Independent from actual composition, $In_xGa_{1-x}As$ is a direct band gap semiconductor, as seen Fig.2.2 which shows the bandstructure of $In_xGa_{1-x}As$, but only $In_{0.53}Ga_{0.47}As$ is lattice matched to InP, while all other combinations are mismatched.[19] The band gap between valence band and conduction band of the lattice matched material is 0.74 eV at 300 K (room temperature). This material system possesses a very high electron mobility, therefore it is well established for semiconductor heterostructures for both electronic and optoelectronic applications and is quite often used for optoelectronic integrated circuits.[19], [9] In this thesis for the fabrication of resonant tunneling diodes, $In_{0.53}Ga_{0.47}As$ was used as well material.

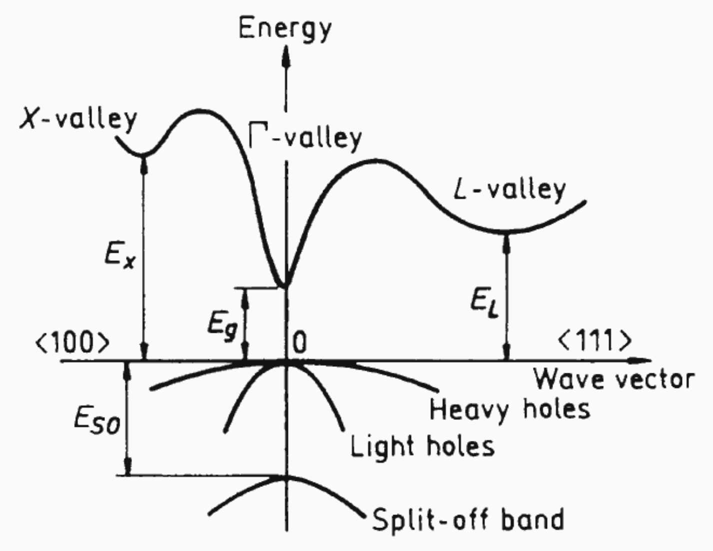

Figure 2.2: Bandstructure of $In_xGa_{1-x}As$.[18]

Selectively chosen parameters of $In_xGa_{1-x}As$ at room-temperature (300 K) can be seen at Tab.2.1. [20]

	$In_{0.53}Ga_{0.47}As$	$In_xGa_{1-x}As$
Crystal structure	Zinc Blende	Zinc Blende
Number of atoms in 1 cm^3	$3.98 \cdot 10^{22}$	$(3.59-0.83x) \cdot 10^{22}$
Lattice constant	5.8687 $\mathring{A}$	(6.0583-0.405x) $\mathring{A}$
Density	5.50 $g \cdot cm^{-3}$	(5.68-0.37x) $g \cdot cm^{-3}$
Dielectric constant (static)	13.9	$15.1-2.87x+0.67x^2$
Dielectric constant (high frequency)	11.6	12.3-1.4x
Effective electron mass m_e	0.041 m_0 (at n= $2 \cdot 10^{17}$ cm^{-3})	$(0.023+0.037x+0.003x^2)$ m_0
Electron affinity	4.5 eV	(4.9-0.83x) eV

Table 2.1: Characteristics of $In_xGa_{1-x}As$

2.1.2 Characteristics and Bandstructure of $GaAs_xSb_{1-x}$

GaAs and GaSb are both direct band gap semiconductors. The material is well researched for $0 < x < 0.3$ and for this specified range, the combined energy gap is defined by $1.42-1.9x+1.2x^2$. State-of-the-art growth of heterostructures is done for x=0.51 (the latticematched combination). For p-doped applications, it is well characterized as base layer of double hetero-bipolar transistors (DHBT's)[21] or for InP based solar cells[22], but as for n-doped usage, more research has to be done to bolster the marginal data already available at the moment. The combination $GaAs_{0.51}Sb_{0.49}$ is lattice matched to InP [9] and used as barriers for the fabrication of resonant tunneling diodes. the bandstructure of GaAs and GaSb is shown in Fig.2.13.

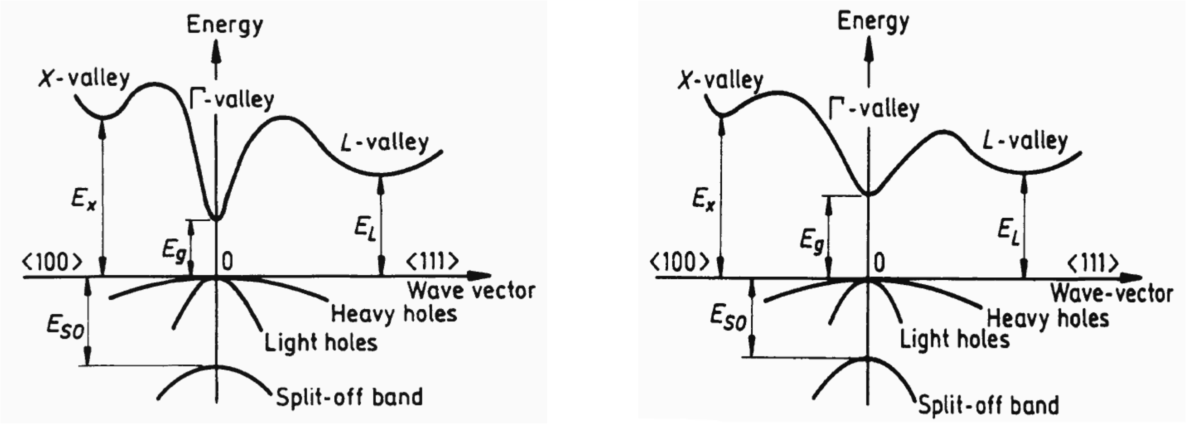
Energy
X-valley
Γ-valley
L-valley
E_x
E_g
E_L
<100>
0
<111>
Wave vector
E_{SO}
Heavy holes
Light holes
Split-off band
Energy
X-valley
Γ-valley
L-valley
E_x
E_g
E_L
<100>
0
<111>
Wave-vector
E_{SO}
Heavy holes
Light holes
Split-off band

(a) Bandstructure of GaAs. (b) Bandstructure of GaSb.

Figure 2.3: Bandstructures of GaAs and GaSb.[18]

For GaAs at room-temperature (300 K), the band gap of the γ-valley is 1.43 eV, while the band gap of the L-valley and X-valley is at 1.71 eV and at 1.90 eV, respectively. For GaSb at room-temperature (300 K), the band gap of the γ-valley is 0.726 eV, while the band gap of the L-valley and X-valley is at 0.81 eV and at 1.03 eV.[18] Table 2.2 shows selectively chosen parameters of GaAs$_{1-x}$Sb$_x$ at room-temperature (300 K)[23]

Crystal structure	Zinc Blende
Number of atoms in 1 cm^3	(4.42-0.89x)$*10^{22}$
Lattice constant	5.65325x + (1-x)$*$6.09593 $\mathring{A}$
Density	(5.32+0.29x) g cm^{-3}
Dielectric constant (static)	12.90 + 2.8x
Dielectric constant (high frequency)	10.89 + 3.51x
Effective electron mass m_e	0.063 - 0.0495x + 0.0258x^2 m_0
Electron affinity	4.07 eV

Table 2.2: Characteristics of GaAs$_{1-x}$Sb$_x$

2.1.3 Characteristics of $In_xGa_{1-x}As/GaAs_xSb_{1-x}$

Both materials $In_xGa_{1-x}As$ and $GaAs_xSb_{1-x}$ can be grown lattice-match to InP with the following composition: $In_{0.53}Ga_{0.47}As/GaAs_{0.51}Sb_{0.49}$. These heterostructures show a type II band alignment.[13], [24] and it is notable that it is an aluminium-free (Al-free) III-V material system. At room-temperature (300 K), the conduction band offset between InP and $In_{0.53}Ga_{0.47}As$ is 0.22 eV, and 0.36 eV between $In_{0.53}Ga_{0.47}As$ and $GaAs_{0.51}Sb_{0.49}$ as can be seen at Fig.2.4. The main promise of this material compound is the relative low effective mass for electrons of $0.043m_0$ for $In_{0.53}Ga_{0.47}As$ and $0.044m_0$ for $GaAs_{0.51}Sb_{0.49}$.[25], [26] This allows improvement of designing electronic devices, especially a possible efficiency boost for quantum-cascade lasers (QCL).[27]

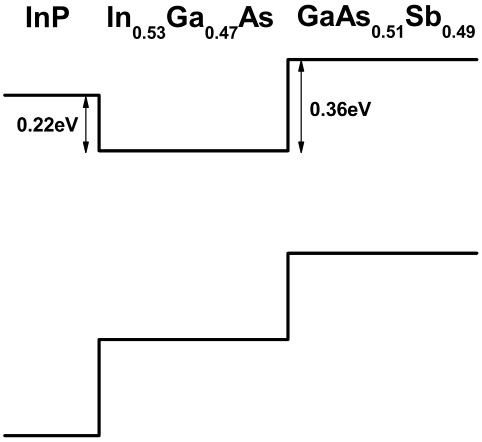

Figure 2.4: Bandstructure of the conduction band and the valence band of InGaAs/GaAsSb. The conduction band offset between $In_{0.53}Ga_{0.47}As$ and $GaAs_{0.51}Sb_{0.49}$ is 0.36 eV.[9]

2.2 Tunneling

In classic physics, every electron is reflected at a potential barrier if the total energy of the electron is lower than the energy of the potential barrier. This is not true anymore, if quantum-mechanics is taken under consideration. To suit quantum-mechanical effects, not only reflection has to be considered, but also a transport phenomenon involving quantum transmission called *tunneling*, has to be taken into account. This means that an electron with a total energy smaller than that of the potential barrier, has also a certain probability to pass through the barrier and so implies a transport possibility through a classical forbidden region. This *tunneling* of carriers, which has typically a rather small, but finite probability, is also often the reason for leakage-currents in high-performance devices.[28] Such a quantum-mechanical tunneling through a potential barrier can be seen in Fig.2.5. Today's state of the art technology allows exact design of the thickness of barriers and as a consequence of this, control the tunneling probability through multiple barriers. This accurate method of growing potential barriers allows to raise the tunneling probability in double-barrier structures for exactly defined energy states.

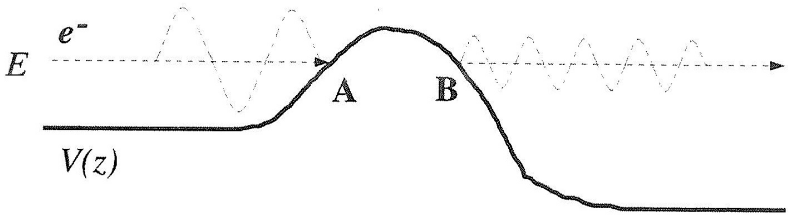

Figure 2.5: Tunneling through a potential barrier for electron energy lower than the energy of the barrier.[12]

A good and common used method to describe the tunneling process of electrons through one or more potential barriers of any kind of semiconductor heterostructures is by using the transfer matrix formalism. The exact calculation method is shown in the next sub-chapter firstly for only a single barrier and afterwards, the results from the single-barrier solution is used and expanded for explanation of a double-barrier structure. The solution for double-barrier structures can again be expanded to be used for a multiple barrier-structures formula algorithm.

2.2.1 Tunneling in Single-Barrier Structures

Symmetric Potential Barrier

To establish a physical background for the transfer matrix formalism, which will be used to characterise the tunneling process, it is essential to start with the Schrödinger equation. The Schrödinger equation provides the mathematical model for motion in quantum mechanics.[29] Equation 2.1 represents the special case for the free particle. In this case, no forces are interfering and the particle possesses constant energy.

$$-\frac{\hbar^2}{2m} * \frac{\partial^2}{\partial x^2} * \psi(x,t) = i * \hbar * \left(\frac{\partial}{\partial t}\right) * \psi(x,t) \tag{2.1}$$

m is the mass of the electron, $\hbar$ is the reduced Planck constant and $\psi(x,t)$ is the time and position depending wave function. Equation 2.2 expands the special case for the free particle into a general one by considering a external potential taking effect on the particle. This is identical to classic physics by defining the sum of the total energy of a particle by adding potential and kinetic energy. Now it is possible to show the general form of the Schrödinger equation for a particle in one direction in space.

$$-\frac{\hbar^2}{2m} * \frac{\partial^2}{\partial x^2} * \psi(x,t) + V(x,t) * \psi(x,t) = i * \hbar * \left(\frac{\partial}{\partial t}\right) * \psi(x,t) \tag{2.2}$$

$V(x,t)$ is the time and position depending potential energy. The last step to achieve the three-dimensional Schrödinger equation is by adding the Laplace-operator to account for all three space dimensions.

$$-\frac{\hbar^2}{2m} * \nabla\psi(\vec{x},t) + V(\vec{x},t) * \psi(\vec{x},t) = i * \hbar * \left(\frac{\partial}{\partial t}\right) * \psi(\vec{x},t) \tag{2.3}$$

with

$$\nabla = \frac{\partial^2}{\partial x^2} + \frac{\partial^2}{\partial y^2} + \frac{\partial^2}{\partial z^2} \tag{2.4}$$

The results of the Schrödinger equation provide wave functions ψ, which have to fulfil certain boundary conditions at any interface between two different regions of potential energy, which are continuousness of the wave-function across the boundary between the two different potential energy regions. This leads to probability waves for transmission and reflection at the boundary, while in classic physics only reflection would occur.

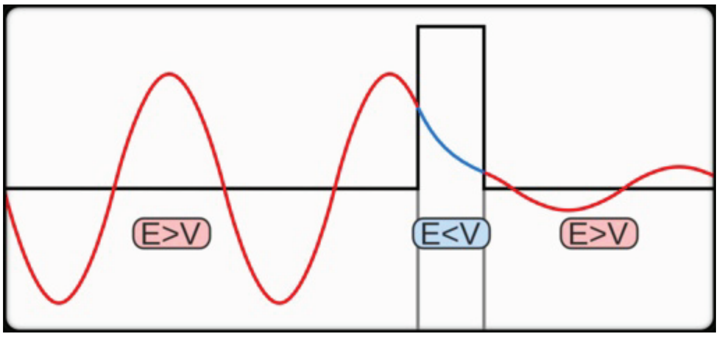

Figure 2.6: The wavefunction is decreasing exponentially inside of a finite barrier.[30]

Fig.2.6 shows, that a wave-function of a particle, arriving from the left of the potential barrier, has exponentially decaying solutions inside the barrier as well as for the right side of the barrier. The important thing is, that these solutions differ from zero. This implicates, that the particle has a finite tunneling probability, which is exponentially decreasing with increasing thickness of the barrier as can be seen in Fig.2.6, for tunneling through the potential barrier and continue its path on the other side. The tunneling probability is, amongst other things, related to the thickness, as mentioned above, but also to the height of the potential barrier and of the effective mass in the barrier.

Starting by considering the time-dependent solution of the Schrödinger equation

$$\psi(\vec{x},t) = exp(-i * \omega * t) * \varphi(\vec{x}) \tag{2.5}$$

together with

$$E = \hbar * \omega \tag{2.6}$$

where E is the energy and ω represents the angular frequency, shows the time-independent Schrödinger equation for a particle

$$-\frac{\hbar^2}{2m} * \nabla\varphi(\vec{x}) + V(\vec{x}) * \varphi(\vec{x}) = E * \varphi(\vec{x}) \tag{2.7}$$

If this equation is used for a real symmetric single-barrier of any kind of material, which is embedded into a another material system for the surrounding regions, like shown in Fig.2.7 and furthermore, only electrons are taken into account which are located in the conduction band of the associated material and incident from the left on the barrier, then the equation can be rewritten into

$$\left(-\frac{\hbar^2}{2m^*(z)} * \frac{\partial^2}{\partial z^2} + V_{eff}(z)\right) * \varphi(z) = E * \varphi(z) \tag{2.8}$$

where m^* is the effective mass. This equation assumes a parabolic dispersion relation and V_{eff} represents the effective potential energy normal to the interface. Here the z-direction is perpendicular to the barriers. Here the conduction band offset ∇ E, associated with the Γ point of the two materials, can be considered as the height of the potential barrier V_{eff}, if space charge effects are marginal and need not be considered. As seen in Fig.2.7, it is possible to differ between the region left of the barrier, the barrier itself and the region right of the barrier.

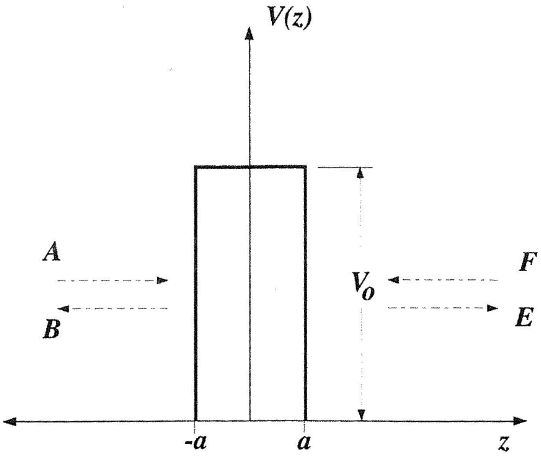

Figure 2.7: Correlation between the transfer matrix coefficients.[12]

For region I and III, the Schrödinger equation shows

$$\frac{\partial^2}{\partial x^2} * \varphi(z) + \frac{2 * m^*}{\hbar^2} * E * \varphi(z) = 0 \tag{2.9}$$

while for region II

$$\frac{\partial^2}{\partial x^2} * \varphi(z) + \frac{2 * m^*}{\hbar^2} * (E - V) * \varphi(z) = 0 \tag{2.10}$$

The solution for the combined function is written as

$$\varphi(z) = \begin{cases} A * e^{i*k*z} + B * e^{-i*k*z} & z < -a \\ C * e^{\kappa*z} + D * e^{-\kappa*z} & -a < z < a \\ E * e^{i*k*z} + F * e^{-i*k*z} & z > a \end{cases} \tag{2.11}$$

where the wavevectors k and κ can be calculated from

$$E = \frac{\hbar^2 * k^2}{2m} \rightarrow k = \sqrt{\frac{2 * m^* * E}{\hbar^2}} \tag{2.12}$$

$$\kappa = \frac{\sqrt{2 * m^* * (V - E)}}{\hbar} \tag{2.13}$$

Incoming and outgoing waves on the left of the barrier are weighted by the coefficient A and B, while E and F are associated with the incoming and outgoing waves on the right side of the barrier. For energies V > E, the solutions of the Schrödinger equation are exponentially rising or decreasing functions inside the potential barrier, depending on the energies of the evanescent states. For energies V < E, the solutions left and right of the barrier are complex exponential solutions as well as for inside the barrier.[12] A concrete possibility to solve this problem will be shown later in this thesis. As said before, the boundary conditions, which guarantee that the envelope function and its derivative are continuously at the interfaces $z = -a$ and $z = a$, will now be used to connect the different incoming and outgoing waves, respectively the coefficients corresponding to the waves, on the right side of the barrier as well as on the left side. Boundary condition for $z = -a$ is

$$\varphi_I(-a_-) = \varphi_{II}(-a_+) \tag{2.14}$$

$$\frac{1}{m^*_-} * \frac{\partial \varphi_I}{\partial z}\bigg|_{-a_-} = \frac{1}{m^*_+} * \frac{\partial \varphi_{II}}{\partial z}\bigg|_{-a_+} \tag{2.15}$$

Further assumption, that the masses m^*_- for the outer edge of the left barrier flank and m^*_- for the inner edge of the left barrier flank are alike, which is the case for the $\text{In}_x\text{Ga}_{1-x}\text{As}$/ $\text{GaAs}_x\text{Sb}_{1-x}$ material system by neglecting a minimal divergence, it is possible to achieve a connection between the coefficients A, B and C, D by using the solutions from Eqn.2.11, to rewrite it to

$$A * e^{-i*k*a} + B * e^{i*k*a} = C * e^{-\kappa*a} + D * e^{\kappa*a} \tag{2.16}$$

$$i * k * [A * e^{-i*k*a} + B * e^{i*k*a}] = \kappa * [C * e^{-\kappa*a} + D * e^{\kappa*a}] \tag{2.17}$$

The same can be done for the boundary conditions on the right side of the barrier $z = a$, which leads to a connection between C, D and E, F.

$$C * e^{\kappa*a} + D * e^{-\kappa*a} = E * e^{i*k*a} + F * e^{-i*k*a} \tag{2.18}$$

$$\kappa * [C * e^{\kappa*a} - D * e^{-\kappa*a}] = i * k * [E * e^{i*k*a} + D * e^{-i*k*a}] \tag{2.19}$$

The coupled coefficients can now be written as matrix-form, which will lead to two matrices, combining the coefficients A, B with C, D as well as for C, D with E, F. These 2 matrices are combined into a new matrix, called *transfer matrix*, coupling directly A, B to E, F.

$$\begin{bmatrix} A \\ B \end{bmatrix} = \begin{bmatrix} M_{11} & M_{12} \\ M_{21} & M_{22} \end{bmatrix} * \begin{bmatrix} E \\ F \end{bmatrix} \tag{2.20}$$

The elements M_{11}, M_{12}, M_{21} and M_{22} are given by

$$M_{11} = [cosh(2 * \kappa * a) - \frac{i}{2} * \left(\frac{k^2 - \kappa^2}{k * \kappa}\right) * sinh(2 * \kappa * a)]exp(2 * i * k * a) \tag{2.21}$$

$$M_{21} = -\frac{i}{2} * \left(\frac{k^2 - \kappa^2}{k * \kappa}\right) * sinh(2 * \kappa * a) \tag{2.22}$$

$$M_{12} = M_{21}^* \ ; \ M_{22} = M_{11}^* \tag{2.23}$$

Under consideration, that the important case is to study only the tunneling probability of an electron, impacting from the left of the barrier, passing through the barrier and continue its path on the right side of the barrier, it is assumable to set the coefficient F to zero which corresponds to no incoming wave from the right side of the structure. Associating the coefficient A to the amplitude of the incoming wave from the left and coefficient E to the transmitted wave on the right, it is possible to couple these waves with the help of the transfer matrix to the transmission coefficient T(E)

$$T(E) = \frac{|E|^2}{|A|^2} = \frac{1}{|M_{11}|^2} \tag{2.24}$$

Under Consideration of Eqn.2.23, it can be written as

$$T(E) = \frac{1}{1 + (\frac{k^2+\kappa^2}{2*k*\kappa})^2 * sinh^2(2 * \kappa * a)} \tag{2.25}$$

Under closer investigation of Eqn.2.25, it is obvious, that the sinh-term will dominate the transmission coefficient, therefore, it must be distinguished between $2 * \kappa * a$ « 1 and $2 * \kappa * a$ » 1. For the case $2 * \kappa * a$ « 1, Eqn.2.25 can be reduced to

$$T(E) = \frac{1}{1 + k^2 * a^2} \tag{2.26}$$

This case represents transmissions through very thin barriers. For the opposite case $2 * \kappa * a$ » 1, which is the most common case, the transmission coefficient T(E) can be written as

$$T(E) = \left(\frac{4 * k * \kappa}{k^2 + \kappa^2} \right)^2 * exp^{-a * \kappa * a} \tag{2.27}$$

In words, Eqn.2.27 shows, that there is a exponentially decrease of the tunneling probability associated to the width of the barrier as well as with the square root of the barrier height.[12] Under consideration of Eqn.2.23, it is also possible to formulate the reflection coefficient on the left side of the barrier by coupling of the coefficients A and B.

$$R(E) = \frac{|B|^2}{|A|^2} = \frac{|M_{21}|^2}{|M_{11}|^2} = |M_{21}|^2 * T(E) \tag{2.28}$$

$$= \frac{(\frac{k^2+\kappa^2}{2*k*\kappa})^2 * sinh(2 * \kappa * a)^2}{1 + (\frac{k^2+\kappa^2}{2*k*\kappa})^2 * sinh(2 * \kappa * a)} \tag{2.29}$$

and obviously

$$T(E) + R(E) = 1 \tag{2.30}$$

At last, all the results above are approved as long as $E < V$. For the case that the electron energy is higher than the actual barrier height, the transmission coefficient T(E) is different, but can be achieved by the same analysis as for $E < V_0$, but κ has to be considered complex as $\kappa = -i * k'$.

$$T(E > V) = \frac{1}{1 + (\frac{k^2-k'^2}{2*k*k'})^2 * sinh^2(2 * k' * a)} \tag{2.31}$$

The transmission probability's for both $E < V$ and $E > V$ is shown in Fig.2.8. The transmission probability is exponentially increasing or decreasing with the energy of the electron, as long as the energy is smaller than the potential energy of the barrier. As soon as the energy of the electron is higher than the height of the potential barrier, the transmission probability is reaching unity by using an oscillating function.[12]

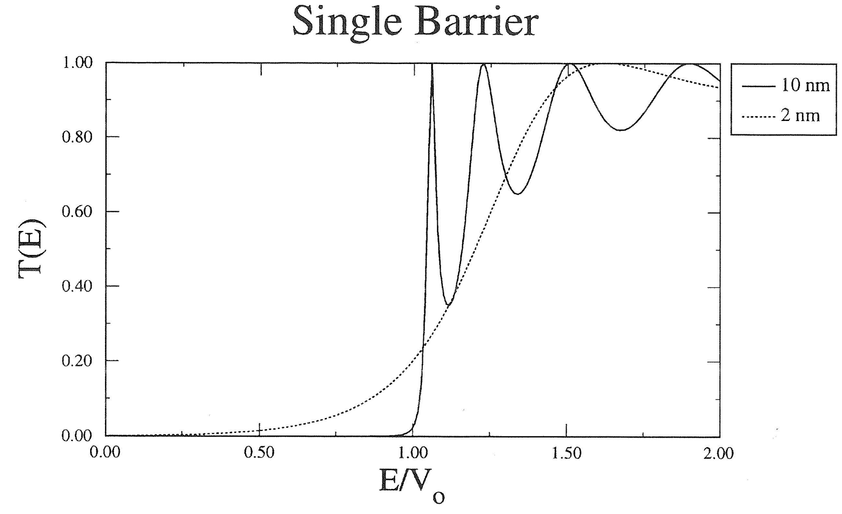

Figure 2.8: Transmission coefficient for a single-barrier structure.[12]

Asymmetric Potential Barrier

The transmission coefficient in case of an asymmetric potential barrier differs from the symmetric barrier coefficient. Nevertheless, the transmission coefficient can be directly derived from the symmetric barrier case by applying a voltage to the right side of the structure. This lead to a biased structure as seen in Fig.2.9.

To be more specific, the transmission coefficient can be calculated as shown for the symmetrical barrier case, but under consideration of different wave-functions which have to be taken into account for the asymmetrical barrier.

$$\varphi(z) = \begin{cases} A * e^{i*k*z} + B * e^{-i*k*z} & z < -a \\ C * e^{\kappa*z} + D * e^{-\kappa*z} & -a < z < a \\ E * e^{i*k_1*z} + F * e^{-i*k_1*z} & z > a \end{cases} \tag{2.32}$$

Under consideration of the new formulated wave-functions and wavevectors k for the left side, κ for the barrier itself and k_1 for the right side, used with the already shown calculation for the symmetric barrier case, the transmission coefficient is written as

$$T(E) = \frac{\frac{4*k_1*k}{(k_1+k)^2}}{1 + \left(\frac{(k^2+\kappa^2)*(k_1^2+\kappa^2)}{\kappa^2*(k_1+k)^2)}\right) * sinh^2 * (2 * \kappa * a)} \tag{2.33}$$

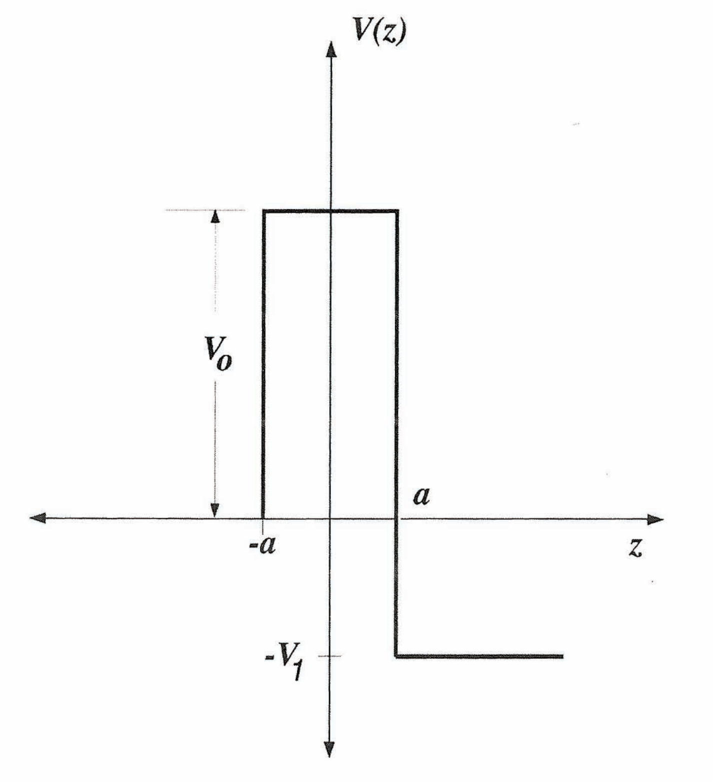

Figure 2.9: Asymmetric single-barrier structure.[12]

2.2.2 Tunneling in Double-Barrier Heterostructures

A model for double-barrier tunneling is based on extending the model for single-barrier tunneling. This is be done, as seen in Fig.2.10, by adding a second barrier to an already existing barrier, forming a double-barrier heterostructure. These two barriers encase a quantum well of defined length. The resulting structure, a quantum-well bordered on each side by a potential barrier, shows the basic heterostructure for the Resonant Tunneling Device (RTD), as seen in Fig.2.10.

As done for single-barrier structures, it is necessary to differentiate between symmetrical, respectively identical barriers, which conform to a RTD without applied bias, and asymmetrical, respectively non-identical barriers, corresponding to a RTD with applied voltage. In conclusion, applied voltage to a RTD will lead to a broken symmetry of the barriers and furthermore, the transmission properties will strongly depend on the applied voltage. Both possibilities of double-barrier structures, containing symmetrical or asymmetrical barriers, can be analysed by using and modifying the already established transfer matrix formalism of the single-barrier structure.

It is now a simple task to obtain the transfer matrices for the first barrier containing the coupling of the coefficients A and B with E and F and also for the second barrier A'and

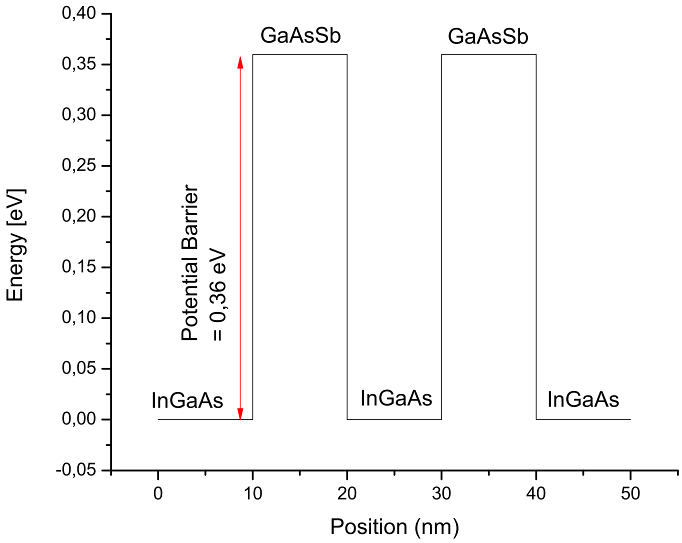

Figure 2.10: InGaAs/GaAsSb double-barrier structure

B'with E'and F'as shown in Fig.2.11. The next step towards the transmission coefficient for a double-barrier heterostructure is to connect the coefficients E and F with A'and B'inside the quantum-well. This is done by

$$A' = E * exp(i * k * b) \tag{2.34}$$

$$B' = F * exp(-i * k * b) \tag{2.35}$$

where b is the thickness of the well and k is the propagation constant inside the well. This equation is easily understood, if considering the uniform potential of the region which leads to only a phase constant difference between the coefficients inside the quantum-well of the two barriers. As done for single-barrier structures, a transfer matrix $\overline{M_W}$ can be defined for the quantum-well. Together with the transfer matrices for the left barrier $\overline{M_L}$ respectively the right barrier $\overline{M_R}$, a composite transfer matrix can be derived, connecting the coefficients A, B to E', F'.

$$\begin{bmatrix} A \\ B \end{bmatrix} = \overline{M_L} * \overline{M_W} * \overline{M_R} * \begin{bmatrix} E' \\ F' \end{bmatrix} = \overline{M_T} * \begin{bmatrix} E' \\ F' \end{bmatrix} \tag{2.36}$$

As well as for the single-barrier case, the inverse square of the coefficient M$_{T11}$ defines the transmission coefficient for the double-barrier case, which can be written as

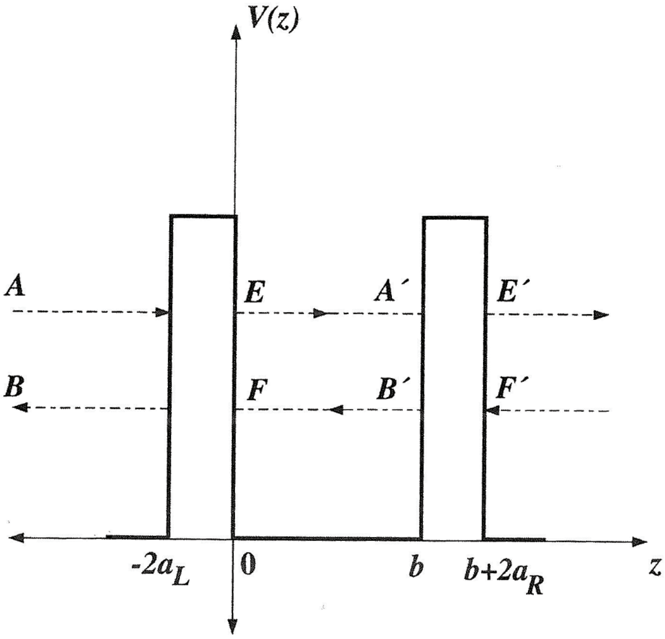

Figure 2.11: Correlation between the transfer matrix coefficients for a symmetric double-barrier structure.[12]

$$M_{T11} = M_{L11} * M_{R11} * exp(-i * k * b) + M_{L12} * M_{R21} * exp(i * k * b) \tag{2.37}$$

The phase factors in Eqn.2.37 define resonance behaviour of the structure by minimizing M$_{T11}$ through elimination of single terms in the equation, leading to possible peaks in the transmission coefficient. Due to the difference of the transmission coefficient T(E) for symmetrical and asymmetrical barriers, both cases have to be discussed separately.

Symmetric Potential Barriers

Considering symmetric, identical barriers, then a few assumptions can be used to simplify the complex transmission coefficient calculation. First, it is assumed that both barriers have the same height as well as the same width. Furthermore, the propagation factor k is the same for all regions and the attenuation constant κ matches inside both of the two barriers. By using the equations, presented for symmetric single-barrier structures before, it is possible to calculate the elements of the transfer matrices $\overline{M_L}$ and $\overline{M_R}$. To show each necessary step would extend the scope of this work, but can be exactly tracked at [12].

Again, the important transfer matrix element is M_{11} which can be written, using polar coordinates, as

$$M_{11} = m_{11} * exp(i * \theta) \tag{2.38}$$

Due to Eqn.2.23, the magnitude m$_{11}$ and the associated phase θ can be defined as

$$m_{11} = \sqrt{cosh^2(2 * \kappa * a) + \frac{k^2 - \kappa^2}{2 * k * \kappa} * sinh^2(2 * \kappa * a)} \tag{2.39}$$

$$\theta = -arctan[(\frac{k^2 - \kappa^2}{2 * k * \kappa}) * tanh(2 * \kappa * a)] + 2 * k * a \tag{2.40}$$

Under consideration of T$_1$ as transmission coefficient and R$_1$ as the reflection coefficient of the single-barrier case, the transmission coefficient can be defined as

$$T_{TOT}(E) = \frac{1}{|M_{T11}|^2} = \frac{1}{1 + 4 * |m_{11}|^2 * |M_{21}|^2 * cos^2(k * b - \theta} \tag{2.41}$$

$$= \frac{T_1^2}{T_1^2 + 4 * R_1 * cos^2(k * b - \theta)} \tag{2.42}$$

The final step is to differentiate between off-resonance state and resonance state. Obviously if the cosine function is unequal to zero, off-resonance state is in service and the lowest transmission coefficient is reached, if

$$k * b - \theta = n * \pi \tag{2.43}$$

In this case the transmission coefficient is written as

$$T_{TOT}^{min} = \frac{T_1^2}{4} \tag{2.44}$$

This leads to the conclusion that the transmission coefficient is much smaller than unity while the reflective coefficient will nearly equal to one. The off-resonance state can be described as a cascaded transmission through the two barriers. On the other hand, if the cosine function of the equation is vanishing, the electron energy is in resonance with the quantum-well state. This is the case, if

$$k * b - \theta = (2 * n + 1)\frac{\pi}{2} \tag{2.45}$$

$$for \quad n = 0, 1, 2, ...$$

The transmission coefficient T_{TOT}^{min} will be nearly unity. This is the case, if the electron energy matches exactly the energy of any *quasi-bound* state inside the quantum-well. Obviously, the perfectly matched energy levels inside the quantum-well and the electron energy is suddenly broken as soon as any kind of asymmetrical behaviour is forced onto the structure, for example by applying bias to the heterostructure, which leads to a shift of the bandstructure.

Asymmetric Potential Barriers

Fig.2.12 shows a double-barrier heterostructure for asymmetric potential barriers.

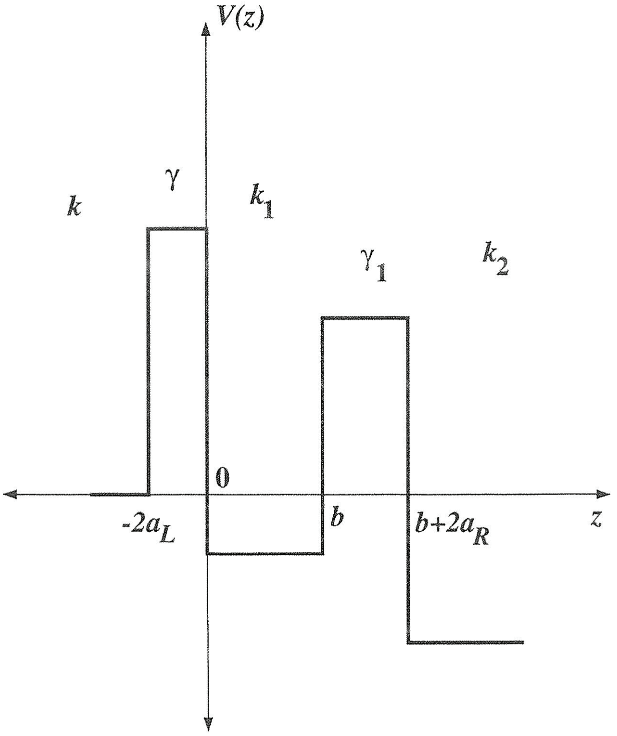

Figure 2.12: Asymmetric double-barrier structure.[12]

As mentioned before, the asymmetric double-barrier structure situation represents the symmetrical double-barrier case with a bias applied to one side of the heterostructure. This applied voltage leads to a shift of the symmetric double-barriers becoming asymmetric. Based on the results of the symmetric double-barrier case and the calculations done for the asymmetrical single-barrier structure, formulating an algorithm to solve asymmetric double-barrier heterostructures as well as to calculate the transmission coefficient can be done. Under consideration of Fig.2.12, it is necessary to use different wave-vectors for each well region of the structure. Furthermore, because of the possibility of different widths and heights for each of the two barriers, it is also necessary to use two different constants κ for each potential barrier. As shown before in the single-barrier case, firstly the transfer matrix elements are defined for the left side and the right side of the barrier. By using polar coordinates again, like shown in the symmetrical double-barrier structure, it is possible to define the matrix elements for the magnitudes m_{L11}, m_{L12}, m_{R11} and m_{R12} as well as the associated phases θ_{L11}, θ_{L12}, θ_{R11}, θ_{R12}.

Using Eqn.2.37 and introducing the newly formulated magnitudes and phases, the matrix element M_{T11} can be derived as

$$\begin{aligned}|M_{T11}|^2 &= (m_{L11} * m_{R11} - m_{L12} * m_{R12})^2 + 4 * m_{L11} * m_{R11} * m_{L12} * m_{R21} \\ &* cos^2 * (k_1 * b + \frac{\theta_{L12} + \theta_{R21} - \theta_{L11} - \theta_{R11}}{2})\end{aligned} \tag{2.46}$$

Finally, the transfer coefficient T(E) can be written, under consideration of the already mentioned and used importance of the matrix element M_{T11} for the calculations for asymmetrical single-barrier structures as well as for symmetrical double-barrier heterostructures as

$$T(E) = \frac{k_2}{k} * \frac{1}{|M_{T11}|^2} = \frac{T_L * T_R}{(1 - \sqrt{R_L * R_R}) + 4 * \sqrt{R_L * R_R} * cos^2(\Phi)} \tag{2.47}$$

with Φ defined as the sum of the phase factors and T_L, T_R, R_L and R_R as the transmission respectively reflection coefficients for the left respectively the right barrier.

2.3 Characteristics of Resonant Tunneling Diodes

For the understanding of the upcoming results in chapter 4 it is necessary to get acquainted with the general behaviour of resonant tunneling diodes. This also includes the contacting of RTDs, because ohmic contacts are a necessity for analysing RTD behaviour without parasitic contact effects.

2.3.1 Ohmic Contacts

For achieving successful fabrication of high-performance semiconductor devices, it is from the utmost importance to process good ohmic contacts between the semiconductor and the metal layers. Ohmic contacts are understood as non-injecting contacts, which provide linear and symmetrical conditions for I-V characterisation, both in forward and reverse bias conditions. This is very important for minimising effects at the contact which complicates the exact extraction of current of semiconductor devices. In contrast to theory, in reality it is not possible to achieve perfect ohmic contacts, so for definition of real ohmic contacts, it is adequate, if the voltage drop inside the bulk semiconductor is much higher than the voltage drop across the contact between the metal and the semiconductor. [31] Tab.2.3 refers to different metallic materials, which form good ohmic contacts combined with semiconductors.

Semiconductor	Metals
Ge (n)	Ag-Al-Sb, Al, Au, Bi, Ai-Au-P, Sb, Pb-Sn
Ge (p)	Ag, Al, Au, Cu, Ga, Ga-In, In, Al-Pd, Ni, Pt, Sn
Si (n)	Ag, Al, Al-Au, Au, Ni, Pt, Sn, In, Ge-Sn, Sb, Au-Sb
Si (p)	Ag, Al, Al-Au, Au, Ni, Pt, Sn, In, Pb, Ga, Ge
GaAs (n)	Au-Ge (88%, 12%)-Ni, Ag-In (95%, 5%)-Ge, Ag-Sn
GaAs (p)	Au-Zn (4%, 16%), Ag-In-Zn, Ag-Zn
InGaAs (n)	Au-Ge, Ni
InGaAs (p)	Au-Zn, Ni
InP (n)	Au-Ge, In, Ni, Sn

Table 2.3: Possible metal semiconductors material combinations for ohmic contacts.[31]

The difference between the band diagrams for Schottky contacts and ohmic contacts are shown in Fig.2.13 as well as a typical I-V curve for ohmic contacts.

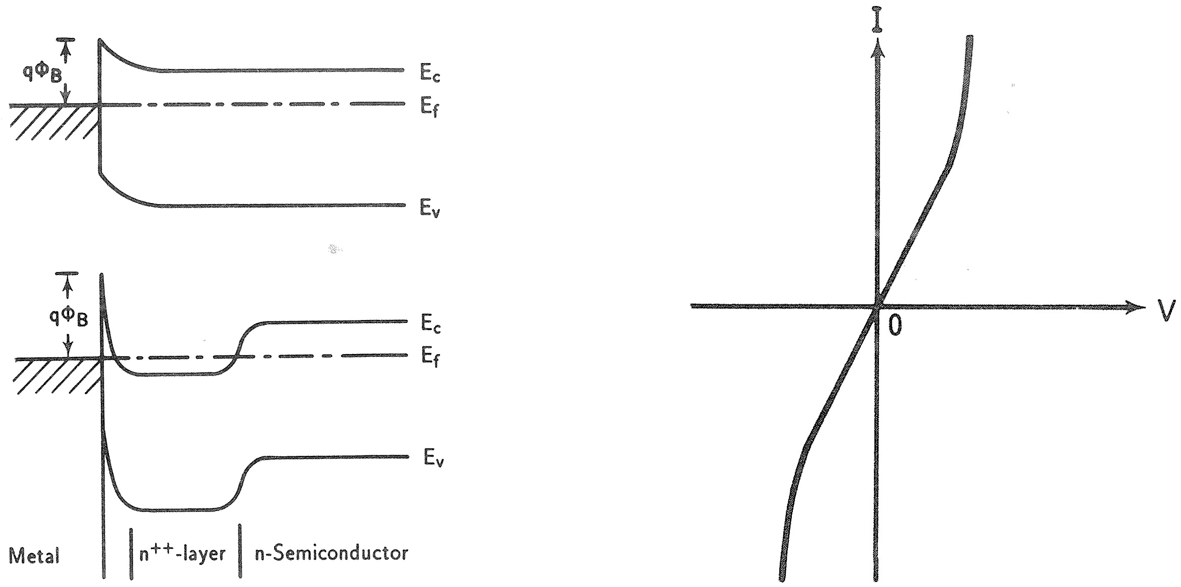

(a) Difference between the energy band of a Schottky contact and an ohmic contact.

(b) I-V characteristic for an ohmic contact.

Figure 2.13: Schottky contact and ohmic contact energy band diagram and I-V of a ohmic contact.[31]

For evaluating ohmic contacts, the specific ohmic resistance R$_c$ is normally used as an characterisation tool. For zero bias, it can be written as

$$R_C = \left(\frac{dJ}{dV}\right)^{-1} \tag{2.48}$$

Under consideration of the applied voltage, the specific ohmic resistance is described as the reciprocal of the derivative of the current density, as shown in Eqn.2.48.[31] To calculate the specific ohmic resistance R$_c$ for differently doped semiconductors, it must be distinguished between medium and heavily doped semiconductors. For medium doped semiconductors, the thermionic process dominates the current through the ohmic contact region of the material. Therefore R$_c$ can be described as

$$R_C = \left(\frac{k_B}{qA * T}\right) exp\left(\frac{q * \phi_{Bn}}{k_B * T}\right) \tag{2.49}$$

where k_B refers to the Boltzmann constant, ϕ_{Bn} to the barrier height, q to the electric charge, T to the temperature and A is associated to the "*effective Richardson constant*"[31].

As for heavenly doped semiconductors, field-emission processes like tunneling are dominating current transport and is mostly depending at doping density [31] and therefore R_C can be calculated as

$$R_C = exp\left[\left(\frac{2\phi_{Bn}}{\hbar}\right) * \sqrt{\frac{\hbar * \epsilon_0 * \epsilon_S * m^*}{N_D}}\right] \tag{2.50}$$

where N_D is the doping density, ϵ_0 is the permittivity of the free space and ϵ_S is the dielectric constant of the semiconductor. Generally, the barrier height of the ohmic contact for a low specific ohmic resistance R_C should be as small as possible. For MBE-doped ohmic contacts, equation 2.50 is satisfied. For alloy contacts, the simplified calculation is not adequate enough any more to describe I-V behaviour across alloyed ohmic contacts [31]. Ohmic contacts are fabricated mostly by evaporation, sputtering or ion implantation and there are various techniques for achieving good metal-semiconductor ohmic contacts, depending on a multiplicity of factors, starting by using p-doped or n-doped semiconductors. Further investigation into this matter would extend the scope of this thesis, but can be studied at [31] in detail.

2.3.2 Basic RTD Quantities

Tsu and Esaki were the first to propose resonant tunneling in semiconductor superlattices in 1973 [32],[11]. Due to its simple structure, the RTD took the role of a fundamental testing device for understanding quantum transport mechanism. This allowed achieving substantial knowledge about quantum-mechanical transport of electrons in semiconductor structures. Based on this gathered informations from extensive RTD testing, it was possible to study and understand more complex quantum-mechanical systems.

Nearly 40 years later, the RTD is still in use to study effects happening during the quantum-mechanical transport. Furthermore, RTDs are used to investigate novel concepts or novel discovered effects, concerning quantum mechanics. During this work, RTDs were used to deepen the understanding of the material system $In_xGa_{1-x}As/GaAs_xSb_{1-x}$ to provide a fundamental base of information for designing more complex structures like quantum cascade lasers on the one hand and to enhance the performance for already existing applications on the other hand.

In addition, RTDs are used in a variety of applications, like they are commonly used as RF oscillators, gates or ultrafast bistable switches.

As mentioned before, RTDs are simple double-barrier heterostructures as seen in Fig.2.14. A quantum well with a defined width is confined on both sides by potential barriers of certain height and width. The well itself and the barriers are normally undoped, but the whole well-barrier-structure is sandwiched between heavily doped contact regions for the collector and the emitter. At a closer look, the heavily doped collector and emitter regions contain degenerate doping to supply a steady large number of electrons, but also forcing the existing flat bands in this highly doped regions to stay flat even under highly applied fields. If this would not be the case, forming space regions would bend the bands and this would consequently result into a number of parasitic effects occurring inside of the device.

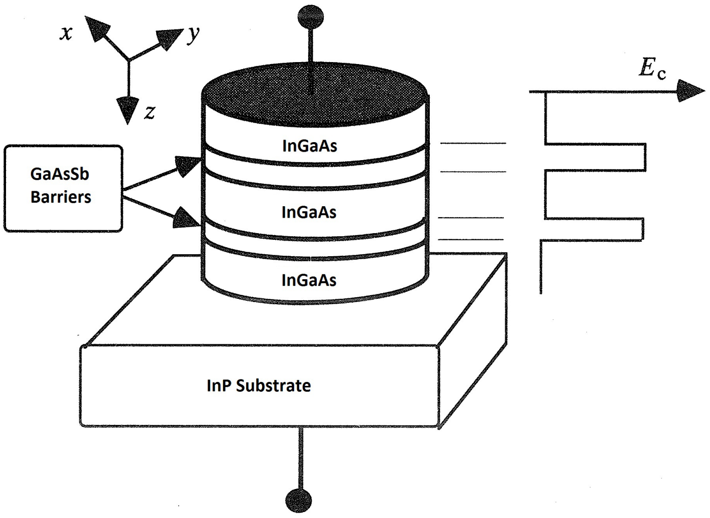

Figure 2.14: Schematic of a InGaAs/GaAsSb RTD. Taken and modified from[33]

Only the *quasi-bound states*, so called *resonant states* which are forming inside the quantum-well, constrain electrons with a certain dwell time, before the electrons escape again. Therefore, every electron inside the well has a probability to tunnel through each of the barriers again. The lifetime τ of the electron is associated with the resonant state, the electron is located in. By usage of the lifetime, an approximation for the width of the resonance energy is possible as $\frac{\hbar}{\tau}$.[12] This concludes that a relevant transmission coefficient is only present at these resonance energy ranges. The range itself is inversely proportional to the corresponding lifetime. The number of those *quasi-bound states* existing inside the well as well as the energies the *quasi-bound states* are occupying, depend on a multiplicity of factors, like the width of the well or the height of the potential barriers.

The basic mechanism of resonant tunneling is shown In Fig.2.15. The Fermi energies E_F^L of the emitter region respectively E_F^R of the collector region are found above corresponding conduction band edges E_C^L and E_C^R. Assumption of a constant electron mass m^* allows to establish the electron supply function as

$$N(E) = \frac{k * T * m^*}{\pi * \hbar} * log[1 + exp(\frac{E_F - E}{k * T})] \tag{2.51}$$

where E_F is the Fermi level and E is the energy. For Fig.2.15 (a), no bias is applied which responds directly to the symmetrical double-barrier case discussed before. The net current actually is zero, because of the of the same amount of current from right to left and left to right which is calculated from

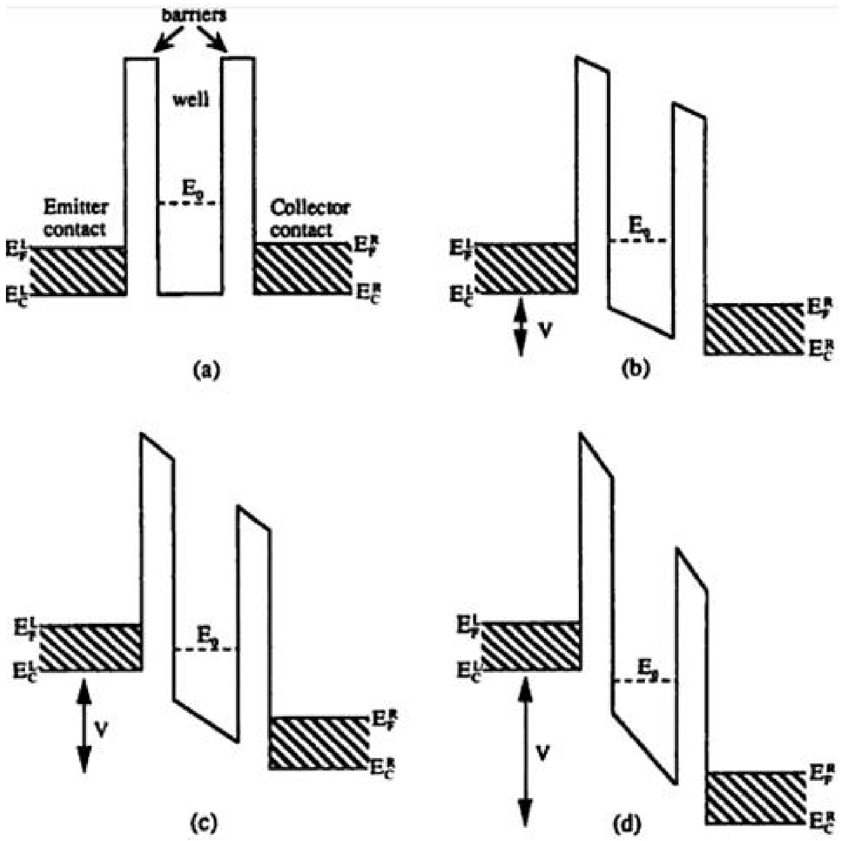

Figure 2.15: Bandstructure of a RTD with applied bias of changing value.[11]

$$j = \frac{e}{2*\pi*\hbar} * \int\limits_{E_{CC}}^{\infty} (T(E)*N_C(E) - T(E)*N_E(E))dE \tag{2.52}$$

where $T(E)$ is the transmission function, E_{CC} is the conduction band edge and e is the electric charge. By using equ.2.51, the current-voltage-characteristic (I-V) is formulated as

$$j = \frac{e*k*T*m^*}{2*\pi^2*\hbar^3} * \int\limits_{E_{CC}}^{\infty} (T(E)*log\left(\frac{1+exp\left(\frac{E_F-E}{k*T}\right)}{1+exp\left(\frac{E_F-E-e*V}{k*T}\right)}\right)dE \tag{2.53}$$

By applying positive bias to the structure, the Fermi Energy on the left side changes and as soon as the Fermi energy coincides to the first resonant state inside the well, the transmission coefficient is largely increased, even nearly to unity with the result of a large current passing through the barriers. Simultaneously, electrons at the Fermi energy on the right side see only a large potential barrier, so the back flow from the right side to the left side is neglectable, which is seen schematically in Fig.2.15 (b) and (c). This is called *resonant tunneling*. As long as the

Fermi-energy equals the energy range of the resonant state inside the well, the dependence of the current on voltage is nearly totally defined by the transmission coefficient. Is the bias further increased, then the lower edge of the conduction band on the left side rises above the upper edge of the energy range of the resonant state inside the well as seen at Fig.2.15 (d), resulting in a decrease of electrons passing through the barrier corresponding to a drop of the transmission coefficient. As a consequence, the resonant tunneling current ceases to flow. This is the so-called *off-resonance state*. Finally for very high bias, the electrons only see a very low height of the right barrier, because of the heavenly altered symmetry of the barriers, which leads to a rising transmission again.

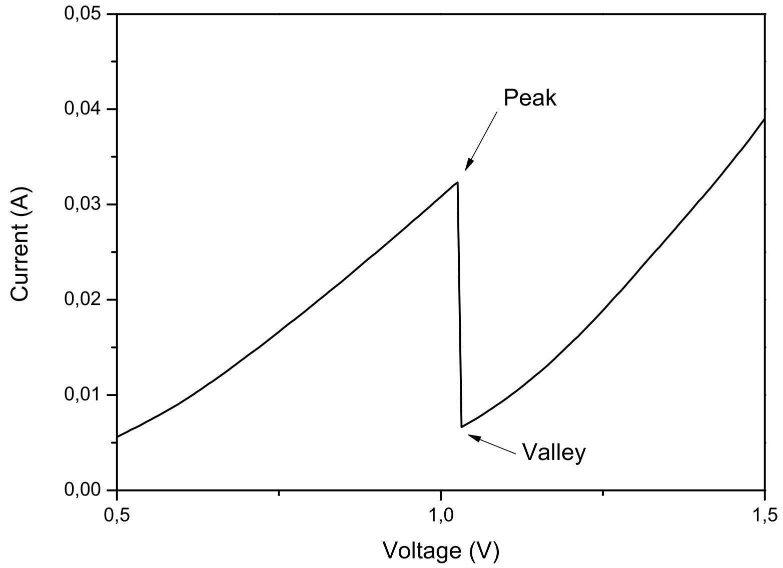

Figure 2.16: Peak-to-valley ratio of a resonant tunneling diode.

An important characteristic value for devices containing negative differential resistance, like the RTD, is the peak-to-valley ratio (PVR). PVR defines the difference between the maximum current at the peak and the minimum current at the valley of a I-V characterisation as shown in Fig.2.16. Typically the PVR decreases with increasing temperature, so that at low temperatures, a higher PVR is measured, while with rising temperatures, NDR is reduced or even completely vanishes depending of the used material and structure.

This temperature depending elution of the peak-to-valley ratio has multiple causes. The obvious one is that as a result of rising temperature also thermionic emission of electrons over the barriers, raises the off-resonant current and also a decrease of peak current is happening as a result of the spreading of the distribution function of the resonant energy levels.[12] A second reason for the vanquishing PVR is that the valley current rising with higher temperatures due inelastic phonon-assisting tunneling through the barriers. This insists that electrons are not brought into the well due to tunneling, but rather because of scattering mechanisms. This has a large impact of the actual valley current and therefore is also a measure for growth quality. The better the growth quality, the less dislocations, impurities or interface disorders are present, leading to only minor influence of the valley current due to scattering and as a result, increasing the actual PVR. Conclusive, for prediction of realistic PVR, considering only coherent processes will lead to false results as there must be also incoherent scattering taken into account. Furthermore, shown by [34] and [35], the relaxation time approximation can be used to sum all scattering effects into one parameter τ. This approximation includes nearly all occurring collision or relaxation processes, like impurity scattering, surface-roughness or electron-electron scattering, allowing derivation of realistic PVR for RTD's and QCL's.

Chapter 3

Fabrication Technologies and Recipes

So far, chapter 1 presented a short outlook of the anticipated results and in chapter 2, after a deeper insight into the material system $In_xGa_{1-x}As/GaAs_xSb_{1-x}$ was given, resonant tunneling diodes physics was presented to better understand the upcoming results. This chapter will address the fabrication of RTDs, beginning with a short excursus on the fabrication technologies in the first part and show detailed fabrication recipes for RTDs, fabricated during this diploma thesis, in the second part.

3.1 Technology for III-V Semiconductor Device Fabrication

To fabricate resonant tunneling diodes, different technology steps are necessary. Starting with the epitaxial growth of the heterostructure using a deposition technique like the molecular beam epitaxy (MBE) or metalorganic vapor phase epitaxy (MOCVD), followed by structuring the grown heterostruscture into a specific number of devices with a defined size on the surface. This is done by using lithography to define the pattern as well as deposition and evaporation techniques like plasma enhanced chemical vapor deposition (PECVD) and reactive ion etching (RIE) to transfer the structures into the grown heterostructures. Finally metal-semiconductor contacts have to be realized by evaporation or sputtering methods.

3.1.1 Molecular Beam Epitaxy

Presently, molecular beam epitaxy (MBE), is an often used technique of growing single crystalline material on the surface of a semiconductor substrate to fabricate ultra-thin semiconductor heterostructures, while allowing a high control of the evaporation process providing sharp interfaces and low background doping. The growth itself is done by depositing one atomic layer after another on the top of a crystalline substrate. For this process to function, an ultra-high vacuum of 10^{-9} to 10^{-10} torr. is needed, which is achieved by a series of pumps.[28]

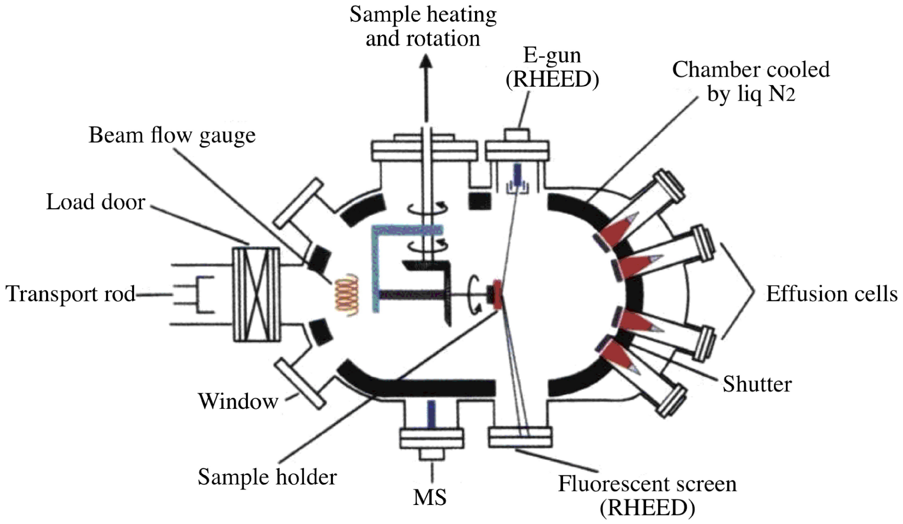

Figure 3.1: Schematic of a typical molecular beam epitaxy growth chamber.[36]

As seen in Fig.3.1, so called Knudsen cells are mounted at one side of the chamber. These cells include refractory crucibles, containing the source material used for the growth of the semiconductor. The crucibles are made of pyrolytic boron nitride (pBN) to prevent interaction with the contained material on the one hand and provide a high thermal stability on the other hand. Through extensive heating, the material inside the crucibles vaporises. This vapor is leaving the Knudsen cell and emitting into the growth chamber. The so formed beam crosses the vacuum chamber until it hits the substrate. The temperature inside the Knudsen cell can be controlled and so the flux rate can be adjusted. Every cell is outfitted with a fast opening respectively closing shutter in front of the orifice, which allows a controlled mono-layer by mono-layer growth of different or combined materials on the surface of the substrate. This defines the composition and the doping of the semiconductor heterostructure at the end of the process. Typical growth rates are 1 to 5 $\mathring{A}$ (15 µm / 24 h), while using substrate temperatures of 450 to 650°C provided by a substrate heater.[37] For example, $\mathrm{In}_x\mathrm{Ga}_{1-x}\mathrm{As}$ and $\mathrm{GaAs}_x\mathrm{Sb}_{1-x}$ were grown at temperatures of 450 to 490°C. The slow growth rates ensure that the deposited monolayers have a high crystalline perfection. As a consequence of the different sticking coefficients of different group elements, for example between group V and group III, it is necessary to adjust the partial pressures of the process. Furthermore to prevent uneven mono-layer growth by geometric variations inside the flux density of the beams, coming from the cells also by different angles (see Knudsen cells in Fig.3.1), the central axis of the substrate holder is rotating. The inner walls of the chamber, surrounding the substrate holder, are cooled down to 78 K by using liquid nitrogen to prevent material in the material beams, that missed the substrate, to reflect and possible disrupt the mono-layer's growth process. One of the biggest advantages of the MBE is the possibility of *in situ* technologies of monitoring and thus controlling the growth and material quality. However the dopant effusion rates are too low to measure *in situ* and thus the doping level still has to be calibrated *ex situ*, e.g. by Hall-effect measurements. An important monitoring tool for observing the fluxes *in situ* is, besides the mass spectrometer, the Reflection High Energy Electron Diffraction(RHEED), which can actually be used while the growth process is running. Fig.3.2 shows the principle working mechanism of the *in situ* control and monitoring technique of RHEED.[37]

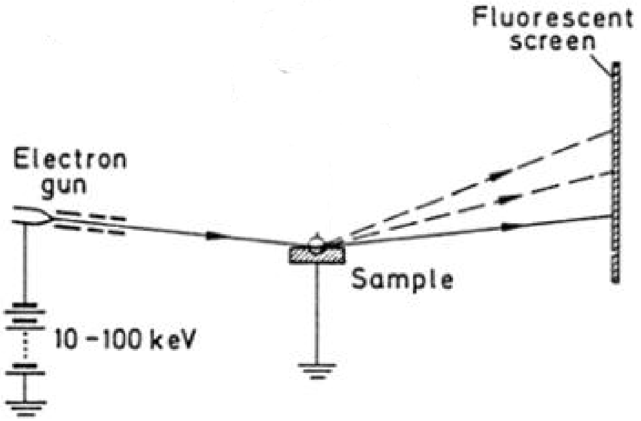

Figure 3.2: Schematic of a RHEED monitoring technique.[38]

Besides the many advantages of molecular beam epitaxy, this method however has the big disadvantage of using ultra-high vacuum technology, which is difficult to handle and has to be re-established after every maintenance or material refilling process.

3.1.2 Plasma Enhanced Chemical Vapor Deposition

The basic principal of chemical vapour deposition (CVD) and plasma enhanced chemical vapour deposition (PECVD), are quite the same. Thin layers are generated by controlled decomposing of gas mixtures on hot surfaces. For this to happen, gas molecules are brought to the hot surface of the substrate and at contact, they split up into an elusive part and an non-elusive part. The none-elusive pieces of the original gas molecule keep on the surface and together with other non-elusive pieces create a new layer on the surface of the substrate, while the elusive parts leak back to the gas mixture inside the CVD reactor and are then pumped out of the gas chamber. Fig.3.3 shows a basic chemical process during a PECVD process.

Through interaction of the temperature on the surface and supplied energy, polycrystalline layers are deposited on the surface of the substrate. CVD and PECVD processes differ in needed temperature and energy supply. In CVD processes, the energy for the process is supplied by temperature, while in PECVD processes, additional energy supply is done electrically

Carrier gas
adsorption on the hot surface
Layer &
Elusive gas

Figure 3.3: Chemical reaction during a PECVD process.

via RF plasma. Plasma enhanced chemical vapour deposition allows depositing a variety of thin films at much lower temperatures than an equal deposition in CVD processes without any loss of the quality of the deposited layers. For example, silicon nitride films, often used as passivation layers in fabrication processes of heterostructure semiconductors, are deposited at only 300°C inside PECVD reactors, while inside CVD reactors temperatures of 700 °C to 900 °C are required. Silane and ammonia are split into silicone nitride and hydrogen as shown below.[39]

$$CVD \qquad 3SiH_4 + 4NH_3 \overset{700°C-900°C}{\longrightarrow} Si_3N_4 + 12H_2 \tag{3.1}$$

Inside the PECVD reactor, which can be seen at Fig.3.4, the electrical energy is transferred into specified gas mixtures with the result of transforming the gas mixture into molecules, reactive radicals and ions. These particles interact with the surface of the heated substrate and create a new layer on the top. The main advantage of PECVD is that this deposition can be achieved at around 300°C, as by the use of RF plasma, the creation of the interacting particles is done inside the gas mixture above the substrate, in contrast to CVD reactors where it is done by varying the temperature.

As semiconductor devices are getting smaller and smaller, the sharp concentration profiles and high position accuracy of structures on the surface of the semiconductors are becoming more and more important. Due to the minimal thermal exposure of chemical vapor deposition or related processes like plasma enhanced chemical vapor deposition during fabrication of these small devices, these processes are increasingly important for manufacturing semiconductors.

3.1.3 Lithography

To cover the whole area of lithography technology would extend the scope of this work by far. Therefore, just a short overview of the existing technologies and methods for pattern-transfer are given. As seen in Fig.3.5, there are different methods in use, each with its own advantages and disadvantages. The most commonly used technique for micro-structures is the photolithography. This technology allows to transfer patters from a photo-mask onto the surface of wafer. This technology was used for fabrication of all samples during this

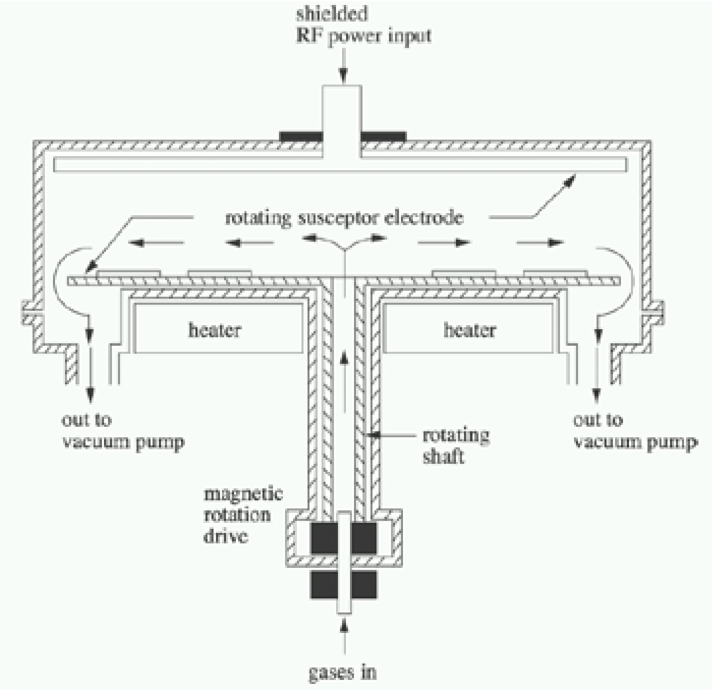

Figure 3.4: Function chart of a PECVD chamber.[40]

thesis. Electron-beam lithography is another lithography technique which is often used for the process of mask fabrication. Furthermore, the techniques of X-ray lithography and Ion-beam lithography are available. Additionally there is also the concept of Nanoimprint technique which again is separated into different techniques like UV nanoimprint lithography or micro-contact printing.[37] Despite of the numerous techniques, the basic concept is more or less the same for all technologies. To create well defined structures on the surface of a wafer, pattern transfer from a photo-mask to a light-sensitive resist on the top of the wafer is done by one of the above mentioned lithography techniques. The resist is deposited by using spin-techniques. After the development is done, the photo-resist contains the structures transferred from the photo-mask. By using deposition or etching methods, these newly formed patterns can be used to create identical structures as of the photo-mask on the wafer. If necessary this step can be repeated several times by using different kind of photo-masks to reshape the whole heterostructure and forming a micro- or even nano-semiconductor device of any kind, like transistors, lasers or resonant tunneling diodes. The selection of the photo-resist is of vital importance for a successful pattern transfer, depending on what kind of devices are to be fabricated. Variation of photo resists are differentiating in positive and negative resists, about to the necessary thickness and by the chemical components the resist contains. The finally chosen technique to transfer the necessary patterns as well as the usage of a well selected photo-resist from a vastly number of obtainable products, is key for a successfully processing.

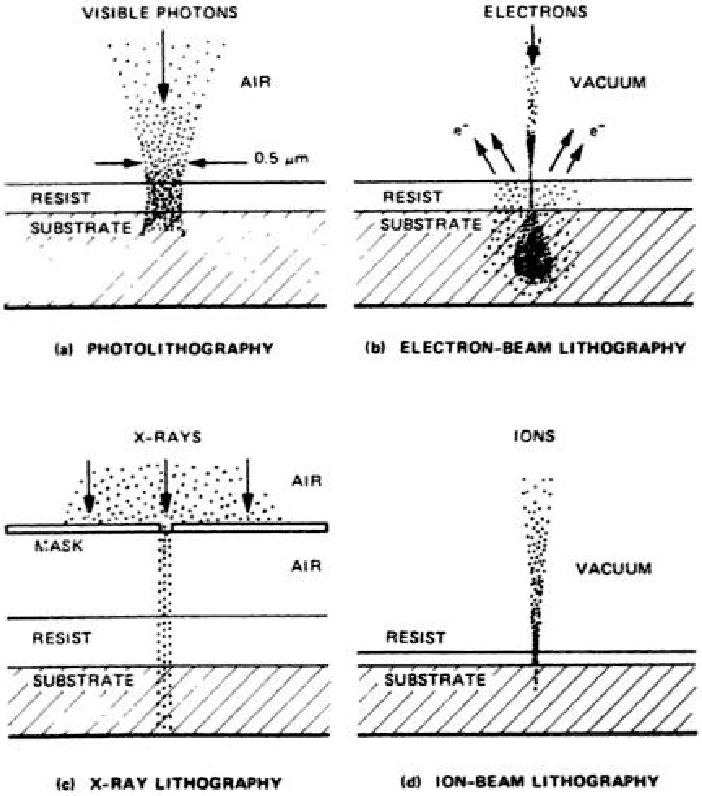
VISIBLE PHOTONS
AIR
0.5 μm
RESIST
SUBSTRATE
(a) PHOTOLITHOGRAPHY
ELECTRONS
VACUUM
e⁻
e⁻
RESIST
SUBSTRATE
(b) ELECTRON-BEAM LITHOGRAPHY
X-RAYS
AIR
MASK
AIR
RESIST
SUBSTRATE
(c) X-RAY LITHOGRAPHY
IONS
VACUUM
RESIST
SUBSTRATE
(d) ION-BEAM LITHOGRAPHY

Figure 3.5: Different lithography technologies.[41]

For further studies, the reader can refer to following books: [37], [39] and [41].

3.1.4 Reactive Ion Etching

There are two different etching methods: wet-etching and dry-etching. As only the dry-etch method of reactive ion etching was used for the fabrication of the resonant tunneling diodes described in this thesis, only the dry-etch method will be described in further detail. Dry ion etching processes are, in comparison to wet-etching, highly anisotropic, which makes it possible to etch nearly vertical side walls. However the dry ion etching technique had the disadvantage of being slow and non-selective. Based on this conclusion, efforts were done to combine the advantages of both methods, like selectivity, speed and anisotropic behaviour, into one single etching system concluding a physical component (ion bombarding) and a chemical component (strongly reactions with the surface material).[42] Consequently, reactive ion etching is based on this principle as shown in Fig.3.6. The different behaviour of anisotropic physical etching and isotropic chemical etching is displayed in Fig.3.7.

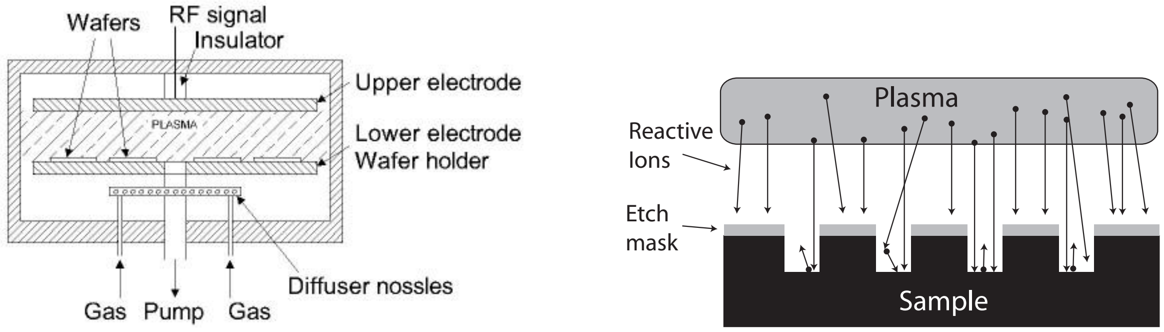

(a) Schematic of the RIE chamber.[43]

(b) Reactive radicals are accelerated towards the surface.[44]

Figure 3.6: Reactive ion etching chamber and working principle.[43],[44]

In principle the PECVD chamber used for the etching is evacuated and then filled with a specified gas mixture. Afterwards a plasma at a frequency of 13.56 MHz is ignited inside of the chamber to generate radicals, which are highly responsive to the material on the surface of the sample. The RF generator is capacitively coupled to the cathode, on which the sample is placed inside the chamber. If a plasma is initiated, a negative potential will be built up at the surface of the sample and then positive reactants inside the plasma will be accelerated towards the surface of the sample. This leads to ion sputtering of the surface material. However not every particle of the gas mixture will be drawn towards the surface. Electrically neutral particles, which are supposedly highly reactive with the material, which should be etched away, are not influenced by the plasma. These particles, which origin from the gas mixture inside the chamber, form the chemical components and have an isotropic etching characterisation on the surface of the sample, while the physical components, ions and electrons, are created in high numbers inside the plasma and then bombard, accelerated by the electrical field, the surface of the sample, having an anisotropic etching characterisation. In this way, the advantages of chemical and physical etching parameters are brought together and are used to transfer nano-metric patterns onto the surface.[42]

Through adjustment of the plasma parameters like radio frequency(RF) power, pressure, and different gas mixtures, it is possible to achieve a highly anisotropic etching process creating nearly vertical side walls, while the chemical component allows a high selectivity between different materials and etch rates. At the end of every etch process, if the necessary film thickness is etched away and a certain over-etch time is reached to ensure, that across the whole surface the material has been removed, the etch process has to be stopped to prevent further etching or eroding of the materials beneath. For this important etch-stop, there are several methods of endpoint detections like residual gas analysing or optical detection.[45]

For the fabrication of resonant tunneling diodes, described in this thesis, optical endpoint

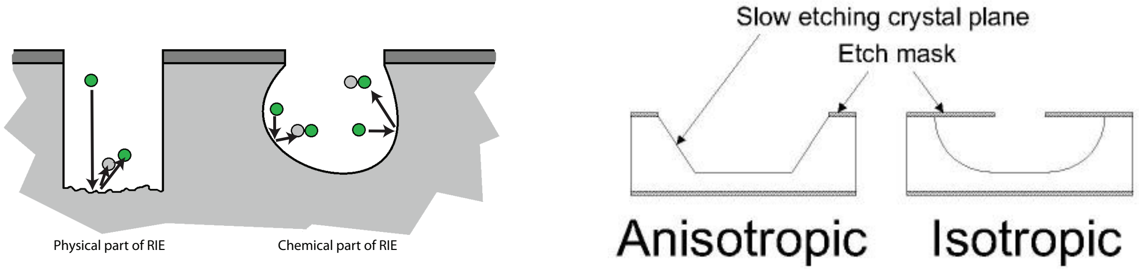

(a) Difference between physical etching and chemical etching.[44]

(b) Etching results of physical etching and chemical etching.[43]

Figure 3.7: Behavior difference between dry-etching and wet-etching.[43],[44]

detection was used. This endpoint detection method is ideal for detecting and monitoring the etch process of multilayer heterostructures. A laser beam with the wavelength of $\lambda_0 = 650$ nm is pointed perpendicular to the sample, this promises high contrast in the different layers refractive indices of the multilayer heterostructure. The laser light is reflected at the bottom and also at the top interface of the layer so that interferences occur. These interacting interferences are depending on the change of the layer thickness during the etch process and they are shown on the monitor as oscillations, with variations depending on the actual film thickness. As soon as the etched layer is completely removed, the oscillations immediately stop as seen at the right side of Fig.3.8, which also shows the etching process and the endpoint detection of a SiN passivation layer. Furthermore, it is possible to etch a certain deep by counting the oscillations and stop the process, if the needed depth is reached even before the layer is completely removed.

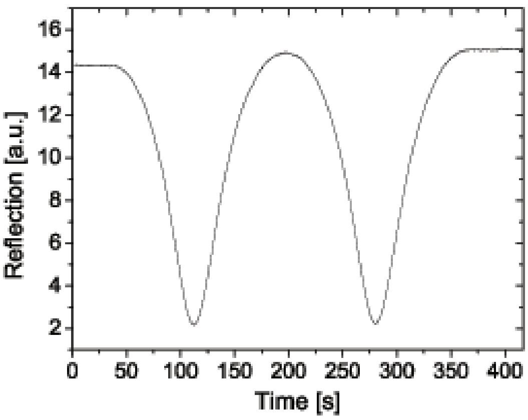

Figure 3.8: Endpoint detection of a SiN passivation layer.[46]

3.1.5 Evaporation

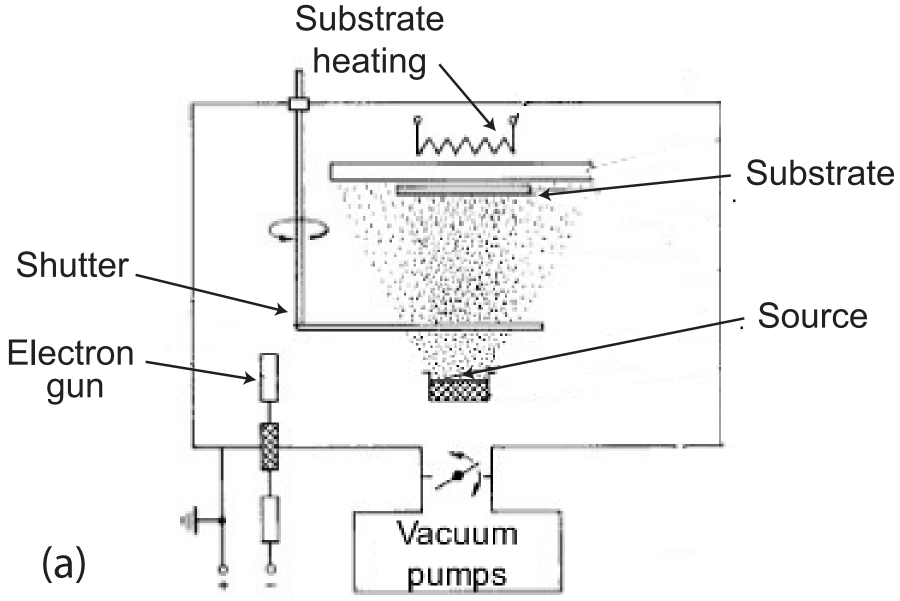

Figure 3.9: Schematic of a evaporation chamber.[46]

Evaporation is a high vacuum method for depositing thin metal or other solid compound films on the surface of a substrate. The evaporation chamber is shown in Fig.3.9 (a). A lot of advantages like a wide range of possible layer thickness, the variety of possible source materials and a great variety of layer adjustments throughout changing the process parameters makes evaporation the most common used method for deposition of metals on semiconductors. A high vacuum of 10^{-8} torr is needed to ensure that the distance between the source and the substrate is much shorter than the mean free path.[47] This guarantees, together with a high purity of the source material, that there is only a small degree of contamination in the deposited layer. In principal, the source material is heated to very high temperatures and evaporates in the evaporation chamber. This can be achieved through direct heating by a resistive heater or an electron beam as seen in Fig.3.9. After the transport of the particles through the chamber, the particles condensate on the surface of the substrate, creating a thin film on top.

Lift-off

Lift-off is a form of area-selective metal deposition, which allows depositing of uniform films of different metals on top of the surface of a substrate. As shown Fig.3.10, through lithography, a structured photo-resist mask is created on the surface. The deposited metal only comes in contact with the actual surface of the substrate, where the resist has been removed through lithography, while the rest of the surface is shielded by the resist. Afterwards the resist can simply be dissolved in a suitable solvent, for example acetone. this solvent also removes the metal film on top of the resist, leaving just the metal on the defined areas of the surface of the substrate. In the end, thermal annealing has to take place, to ensure good adhesion of the deposited metal and the semiconductor surface.

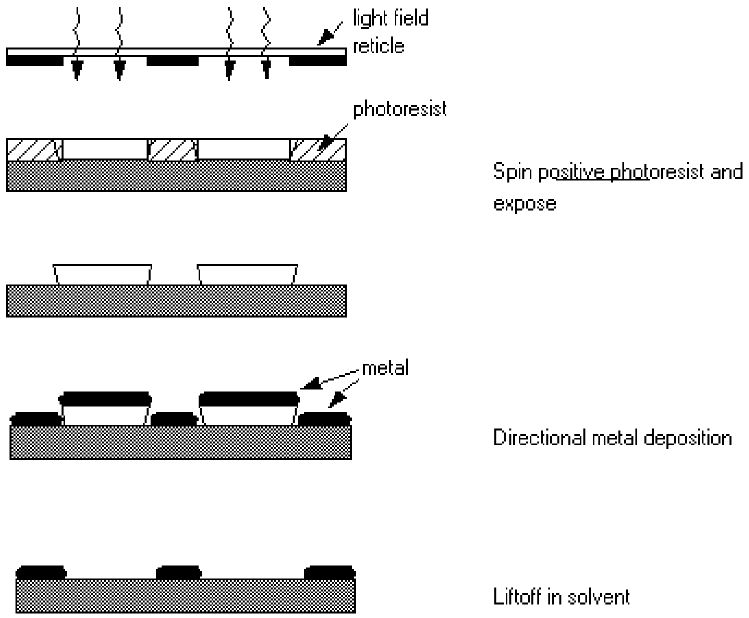
light field reticle
photoresist
Spin positive photoresist and expose
metal
Directional metal deposition
Liftoff in solvent

Figure 3.10: Process steps of the Lift-Off process.[48]

3.1.6 Sputtering

Sputtering is another plasma based technique and is often used for deposition of metallization layers. Different target materials, like gold, or titanium are placed on top of a cathode, which then accelerates noble gas ions towards the target. The ions impact on the surface and thus remove material particles, creating a vapor by vaporizing these particles. After transport through the chamber, the vapour condense on the surface of the substrate, which is heated. Compared to evaporation, in order to reach a maximum number of target atoms condensate on the surface of the substrate using this method, the distance between the target and the substrate is only a few centimetres. Also the energy is much higher, between 3 eV to 10 eV, than as atoms have in evaporation, which is around 0,2 eV.[45] Furthermore sputtering is a more isotropic deposition than evaporation is, because due to collision with gas particles, the target particles hit the substrate surface from various angles, guaranteeing good coverage of the whole surface, including sidewalls of etched structures.

The creation of the ions is done through plasma discharge, which is happening between the two electrodes inside the sputtering chamber. Often Argon is used as gas molecules and

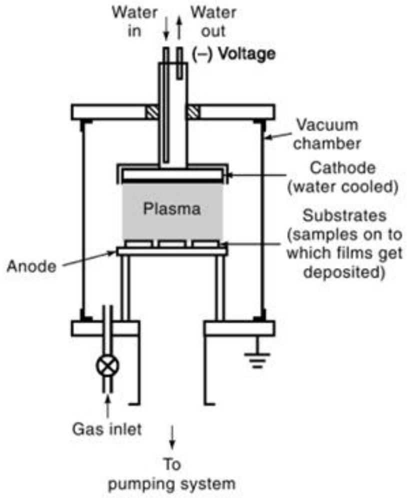
Water in
Water out
(–) Voltage
Vacuum chamber
Cathode (water cooled)
Plasma
Substrates (samples on to which films get deposited)
Anode
Gas inlet
To pumping system

Figure 3.11: Schematic of a sputtering system.[49]

through collision between the gas molecules and the free electrons ionization occurs. An electric field is applied between the anode and the cathode inside the chamber, accelerating Ar ions towards the target and on collision, kinetic energy is passed from the Ar-ions towards the atoms inside the target atomic lattice. These atoms can leave the lattice, if the energy provided by the Ar-ions is greater than the surface binding energy. The so called sputtering yield is given by

$$S = \frac{number\ of\ removed\ target\ atoms}{number\ of\ colliding\ ions}$$

This yield is angle depending, with the highest sputter yield at 60 °C.[45] Sputter yields for a variety of materials as well as the dependence of the ion energy E_i are shown in Fig.3.12.

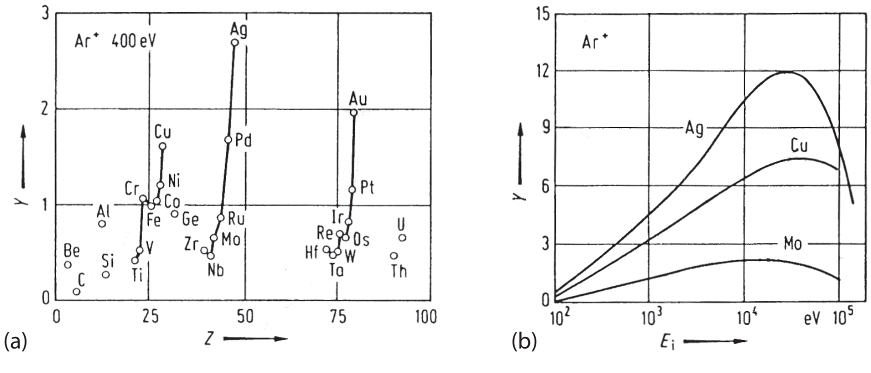

Figure 3.12: Sputter yield Y for different target materials and the dependence of the ion energy of 400 eV.[50]

There are different sputtering methods in use, like DC Sputtering, HF Sputtering, Bias Sputtering, Reactive Sputtering and Magnetron Sputtering.[45] To summarize the three deposition technologies presented in this thesis, Fig.3.13 shows the main differences in deposition techniques of the presented technologies.

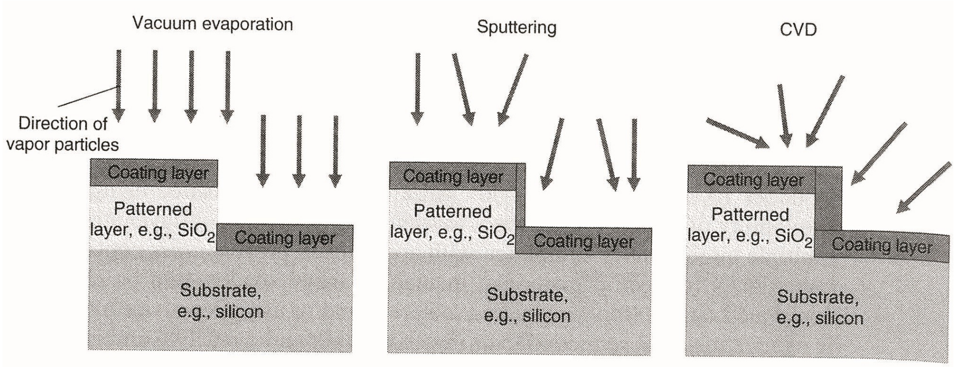
Vacuum evaporation
Direction of vapor particles
Coating layer
Patterned layer, e.g., SiO_2
Coating layer
Substrate, e.g., silicon
Sputtering
Coating layer
Patterned layer, e.g., SiO_2
Coating layer
Substrate, e.g., silicon
CVD
Coating layer
Patterned layer, e.g., SiO_2
Coating layer
Substrate, e.g., silicon

Figure 3.13: Comparison of different deposition technologies.[45]

3.2 Fabrication Recipes of Processed Resonant Tunneling Diodes

All resonant tunneling diodes, which have been fabricated for this diploma thesis, were entirely made in the clean-room of the Zentrum für Mikro- und Nanostrukturen (ZMNS), at the Vienna University of Technology. The processing started by depositing of a SiN passivation layer on top of a heterostructure grown in the solid source molecular beam epitaxy(MBE), Riber R32P, via plasma enhanced chemical vapour deposition (PECVD), in the Oxford Plasmalab 80 Plus System. The composition of the heterostructure will be explained in detail later on in this thesis. Followed by different lithography steps, which were all done by using the mask-aligner MJB3 "Karl Süss", during the whole fabrication process. Afterwards reactive ion etching(RIE), was used to structure the devices via Oxford Instruments Plasmalab System 100. All lithography steps in the following process descriptions, as mentioned before, were made by using the mask-aligner MJB3 "Karl Süss", which emits a power of 12 mW/cm_2.

Two different masks for alignment, used for each lithography step during the processing, were used for the fabrication process. This was necessary to ensure the fabrication of different device sizes and device structures. This point however will be explained in more detail later on in this chapter. The mask, used for the first process recipe, allowed to create RTD's of 100µm x 100µm , 30µm x 30µm and 10µm x 10µm. For devices bigger then 10µm x 10µm the last process step would be a metallisation step via vapor deposition for electrical connectivity done in the Leybold vapour deposition system. For devices smaller then 10µm x 10µm, more processing steps were needed for the implementation of extended pads for contacting the structures. These additional steps contained another lithography step and etching process as well as sputtering for the final contact layer by a Von Ardenne LS320S system.

As mentioned before, for the experimental part of this thesis, there were two different lithography masks used. The mask *"Coquelin"*, as seen in Fig.3.14, containing devices sizes of 100µm x 100µm , 30µm x 30µm and 10µm x 10µm, was used at the beginning of the practical part to primary test the functionality of the new material system InGaAs/GaAsSb by using resonant tunneling diodes and to evaluate what to expect from the material. This process is described in detail in sub-chapter *processing 1*.

To investigate the samples further on, the second mask *"Golka"*, as seen in Fig.3.15, was used to reduce the size of the devices to 40µm x 40µm, 10µm x 10µm , 5µm x 5µm, 4µm x 4µm and 3µm x 3µm. Unfortunately the mask was not originally designed for this kind of research process, so there were alignment problems to overcome during the lithography steps in the fabrication process. Alignment test-runs were made to achieve the highest possible success in processing smaller devices. The results of the alignment testing showed, that the best performance could be created by just using device sizes of 40µm x 40µm , 10µm x 10µm and 5µm x 5µm. The processing steps for the fabrication of these devices are specified in the sub-chapter *processing 2*.

After the final step for both fabrication processes, all samples were cleaved to 3 mm x 5 mm pieces to fit into *"Dual In-Line (DIL)"*-casing for bonding and further measurement outside of the clean-room.

3.2.1 Processing 1 - RTD size: 100µm x 100µm, 30µm x 30µm, 10µm x 10µm

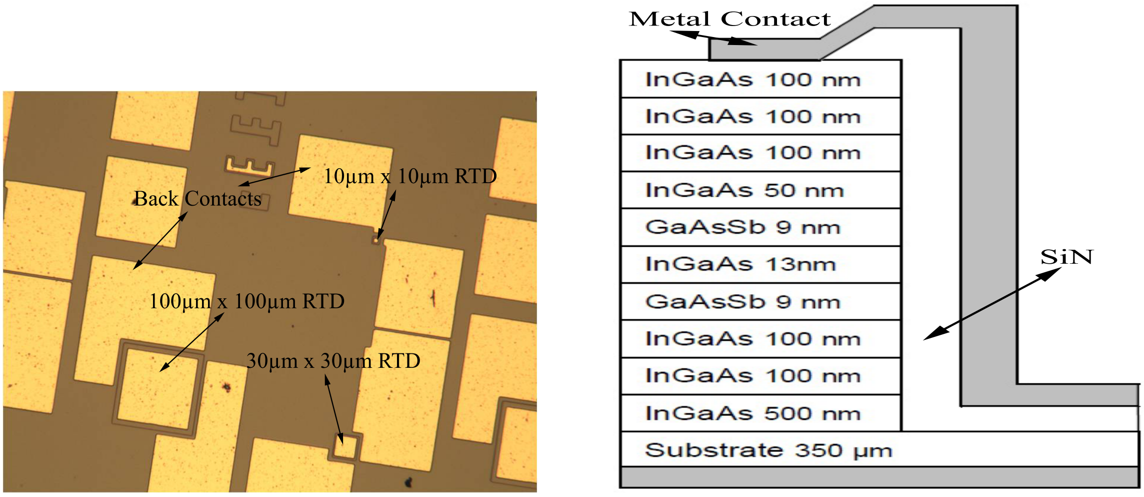
10µm x 10µm RTD
Back Contacts
100µm x 100µm RTD
30µm x 30µm RTD
Metal Contact
InGaAs 100 nm
InGaAs 100 nm
InGaAs 100 nm
InGaAs 50 nm
GaAsSb 9 nm
InGaAs 13nm
GaAsSb 9 nm
InGaAs 100 nm
InGaAs 100 nm
InGaAs 500 nm
Substrate 350 µm
SiN

(a) Structures of Mask *"Coquelin"* (b) Scheme of fabricated RTD with contacts

Figure 3.14: Fabrication mask for *Processing 1* and scheme of fabricated RTD.

1. PECVD (180nm SiN)

   SiH_4 : 700 sccm ; NH_3 : 18 sccm ; Process Power : 12 W ; Pressure : 1 torr.
   Temperature : 300 °C ; Time : 15 min ; Thickness : 180 nm

2. Lithography Mesa

   - Photo resist

     HMDS : 4000 rpm @ 35s ; Baking Process : 120°C @ 60s
     5214 1:1 : 4000 rpm @ 35s (350nm) ; Baking Process : 100°C @ 60s

   - Lithography Edge Removal

     Exposure : 15s ; MIF726 : 30s / 10s / 10s

   - Lithography Mesa

     Exposure : 6s ; MIF726 : 15s / 10s / 10s

3. RIE (SiN hard-mask etching and deep-etching of the heterostructure)

   - Hard-mask

     SF_6 : 40.0 sccm ; NH_3 : 15.0 sccm ; Strike Pressure : 40.0 torr.
     Temperature : 30 °C ; RF : 60 W ; Time : 2-3 min

- O_2-process for photo resist softening

  O_2 : 50.0 sccm ; Pressure : 15.0 torr. ; Strike Pressure : 40.0 torr.
  Temperature : 30 °C ; RF : 80 W ; Time : 10 min ; ICP : 100 W

  Alternatively, it is also possible to use the Plasma Oxidizer for photo resist softening (12 min @ Pressure : 0,75)
- Photo resist removal with Aceton & Isopropanol

4. Deep-etching ($SiCL_4$ & Ar)

   - Deep-etching process

     Needed depth for highly doped layer: 650 to 700 nm or 880 nm, if the Sin-layer is also accounted for. Etchrate is around 1.3 nm/s.

     $SiCl_4$: 5.0 sccm ; Ar : 40.0 sccm ; Pressure : 2.0 torr. ; Strike Pressure : 40.0 torr.
     Temperature : 250 °C ; RF : 100 W ; Time : 7-10 min ; ICP : 0 W ; Wafer : Si
   - Removal of SiN hard-mask

     SF_6 : 40.0 sccm ; Pressure : 15.0 torr. ; Strike Pressure : 40.0 torr.
     Temperature : 30 °C ; RF : 60 W ; Time : 80-90 s ; ICP : 0 W

5. Lithography Ohmic

   - Photo resist

     5214 1:0 : 9000 rpm @ 35s (670nm) ; Baking Process : 100°C @ 60s
   - Lithography Edge Removal

     Exposure : 15s ; MIF726 : 30s / 10s / 10s
   - Lithography Ohmic

     Image-Reversial-Process : 9s / 120°C @ 60s / 17s ; MIF726 : 25s / 10s / 10s

6. Vapor Deposition (Ge-Au-Ni-Au)

   The samples were either glued with photo-resist or fixed by using *"Kohlepads"* on glass plates.

   - Vapor Deposition

     Ge : 150 A (15nm) ; Au : 300 A (30nm) ; Ni : 140 A (14nm) ; Au : 1500 A (150nm)
   - Lift off using Aceton & Isopropanol

7. Extended Pads

   Extended pads are only needed in case of measuring device sizes of 30 µm x 30 µm and 10 µm x 10 µm. For device sizes of 100 µm x 100 µm, only a final annealing step is necessary.

   - Final annealing step for fabrication processes without extended pads

     Program : *Mujagic-365-120* ; Temperature : 365 °C ; Time : 120 s

   If extended pads are needed, the following steps have to be done:

   - PECVD 300nm SiN

     SiH_4 : 700 sccm ; NH_3 : 18 sccm ; Process Power : 12 W ; Pressure : 1 torr.
     Temperature : 300 °C ; Time : 25 min ; Thickness : 180 nm

- Lithography Isolation
  - Photo-resist
    5214 1:0 : 9990 rpm @ 35s (1um) ; Baking Process : 100°C @ 60s
  - Lithography Edge Removal
    Exposure : 15s ; MIF726 : 30s / 10s / 10s
  - Lithography Isolation
    Exposure : 7s ; MIF726 : 15s / 10s / 10s
- RIE (SiN hard-mask etching)
  - Hard-mask
    SF_6 : 40.0 sccm ; NH_3 : 15.0 sccm ; Strike Pressure : 40.0 torr.
    Temperature : 30 °C ; RF : 60 W ; Time : 2-3 min
  - O2-process for photo-resist softening
    O_2 : 50.0 sccm ; Pressure : 15.0 torr. ; Strike Pressure : 40.0 torr.
    Temperature : 30 °C ; RF : 80 W ; Time : 10 min ; ICP : 100 W
    Alternatively, it is also possible to use the Plasma Oxidizer for photo resist softening (12 min @ Pressure : 0,75)
  - Photo-resist removal with Acetone & Isopropanol
- Lithography Sputtering
  - Photo-resist
    5214 1:0 : 9990 rpm @ 35s (1um) ; Baking Process . 100 °C @ 60s
  - Lithography Edge Removal
    Exposure : 15s ; MIF726 : 30s / 10s / 10s
  - Lithography Ohmic
    Reversial-Process : 9s / 120°C @ 60s / 17s ; MIF726 : 25s / 10s / 10s
- Sputter (Ti-Au)
  - Sputtern
    Ti : 50 W @ 3 x 30 s ; Au : 25 W @ 15 x 40 s
  - Lift-Off with Acetone & Isopropanol
- Annealing
  - Annealing
    Program : *Mujagic-365-120* ; Temperature : 365 °C ; Time : 120 s

3.2.2 Processing 2 - RTD size: 40µm x 40µm, 10µm x 10µm, 5µm x 5µm

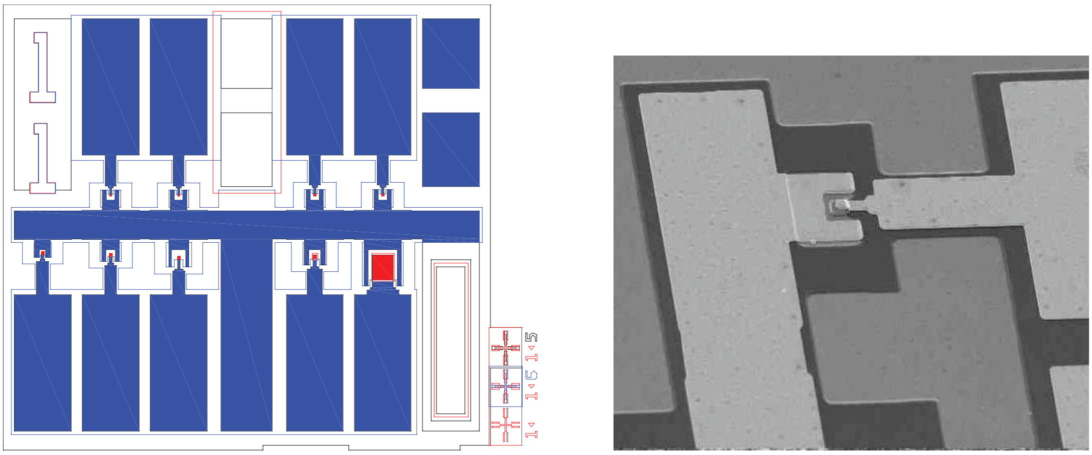

(a) Mask *"Golka"*. Red colored regions show the 40µm x 4µm, 10µm x 10µm and 5µm x 5µm RTDs and blue colored regions represents the metalic contacts

(b) Image of fabricated RTD with contacts

Figure 3.15: Fabrication mask for *Processing 2* and image of fabricated RTD.[51]

1. PECVD (180nm SiN-layer)

   SiH_4 : 700 sccm ; NH_3 : 18 sccm ; Process Power : 12 W ; Pressure : 1 torr.
   Temperature : 300 °C ; Time : 15 min ; Thickness : 180 nm

2. Lithography Mesa

   - Photo-resist

     HMDS : 4000 rpm @ 35s ; Baking Process : 120°C @ 60s
     5214 1:1 : 9000 rpm @ 25s (220nm) ; Baking Process : 100°C @ 60s

   - Lithography Edge Removal

     Exposure : 15s ; MIF726 : 25s / 10s / 10s

   - Lithography Mesa

     Reversial-Process : 9s / 120°C @ 60s / 16s ; MIF726 : 25s / 10s / 10s

3. RIE (SiN hard-mask etching and deep-etching of the heterostructure)

   - Hard-mask

     SF_6 : 40.0 sccm ; NH_3 : 15.0 sccm ; Strike Pressure : 40.0 torr. ; Temperature : 30 °C
     RF : 60 W ; Time : 2-3 min

   - O_2-process for photo-resist softening

     O_2 : 50.0 sccm ; Pressure : 15.0 torr. ; Strike Pressure : 40.0 torr.
     Temperature : 30 °C ; RF : 80 W ; Time : 10 min ; ICP : 100 W

     Alternatively, it is also possible to use the Plasma Oxidizer for photo resist softening (12 min @ Pressure : 0,75)

- Photo-resist Removal with Acetone & Isopropanol

4. Deep-etching ($SiCL_4$ & Ar)

    - Deep-etching process
      $SiCl_4$: 5.0 sccm ; Ar : 40.0 sccm ; Pressure : 2.0 torr. ; Strike Pressure : 40.0 torr.
      Temperature : 250 °C ; RF : 100 W ; Time : 7-10 min ; ICP : 0 W ; Wafer : Si

      Needed depth for highly doped layer: 650 to 700 nm or 880 nm, if the Sin-layer is also accounted for. Etchrate is around 1.3 nm/s.

    - Removal of SiN hard-mask
      SF_6 : 40.0 sccm ; Pressure : 15.0 torr. ; Strike Pressure : 40.0 torr.
      Temperature : 30 °C ; RF : 60 W ; Time : 80-90 s ; ICP : 0 W

5. PECVD (Isolationlayer SiN (R188,R189 SiN) 300nm)

   SiH_4 : 700 sccm ; NH_3 : 18 sccm ; Process Power : 12 W ; Pressure : 1 torr.
   Temperature : 300 °C ; Time : 25 min ; Thickness : 300 nm

6. Lithography Isolation (R188,R189 SiN)

   The photo-resist should have a height of around 700 nm to equal the height of the Mesa. To achieve this, several photo-resist mixtures have been tested. The results are shown in Fig.3.16 and Tab.3.1.

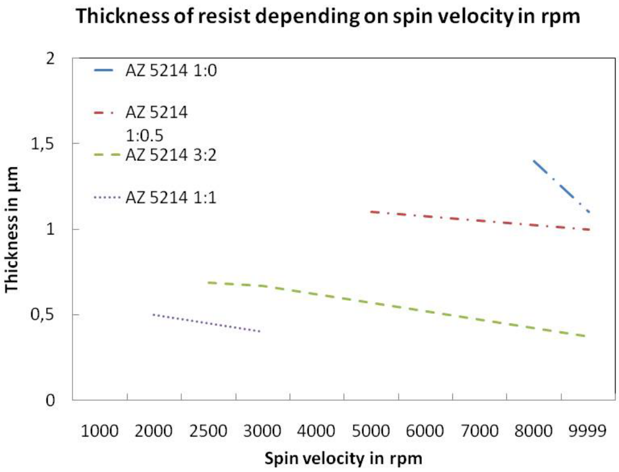

Figure 3.16: Trends for different mixing ratios of the photo-resist AZ 5214 associated to variations of the spin velocity.

- Photo-resist
  5214 3:2 : 3000 rpm @ 35s (670nm) ; Baking Process : 100°C @ 60s
- Lithography Edge Removal
  Exposure : 15s ; MIF726 : 25s / 10s / 10s

photo-resist	rpm	time	thickness
5214 1:0	9900	35	1,1um
5214 1:0	8000	35	1,4um
5214 1:1	3000	35	400nm
5214 1:1	2000	25	500nm
5214 1:0,5	9900	35	1um
5214 1:0,5	5000	35	1,1um
5214 3:2	9000	35	370nm
5214 3:2	3000	35	670nm
5214 3:2	2500	35	685nm

Table 3.1: Thickness of the different resist mixtures of AZ5214 depending on the spin velocity.

- Lithography Isolation
  Reversial-Process : 9s / 120°C @ 60s / 17s ; MIF726 : 25s / 10s / 10s

7. RIE Isolationlayer etching (hardmask) (R188,R189 SiN)
   - Hard-mask
     SF_6 : 40.0 sccm ; Pressure : 15.0 torr. ; Strike Pressure : 40.0 torr.
     Temperature : 30 °C ; RF : 60 W ; Time : 60-90 s
   - O_2-process for photo-resist softening
     O_2 : 50.0 sccm ; Pressure : 15.0 torr. ; Strike Pressure : 40.0 torr.
     Temperature : 30 °C ; RF : 80 W ; Time : 10 min ; ICP : 100 W
   - Removal of photo-resist with Acetone & Isopropanol

8. Lithography Metal
   - Photo-resist
     5214 1:0 : 9000 rpm @ 35s (1,2um) ; Baking Process : 100°C @ 60s
   - Lithography Edge Removal
     Exposure : 15s ; MIF726 : 25s / 10s / 10s
   - Lithography Metal
     Reversial-Process : 9s / 120°C @ 60s / 17s ; MIF726 : 25s / 10s / 10s

9. Vapor Deposition (Ge-Au-Ni-Au)
   The Probes were either glued with photo-resist or fixed by using *"Kohlepads"* on glass plates.
   - Vapor Deposition
     Ge : 150 A (15nm) ; Au : 300 A (30nm) ; Ni : 140 A (14nm) ; Au : 1500 A (150nm)
   - Lift-Off with Acetone & Isopropanol

10. Annealing
    - Annealing
      Program : *Mujagic-365-120* ; Temperature : 365 °C ; Time : 120 s

Chapter 4

Characterisation of Resonant Tunneling Diodes

So far, the necessary theoretical background for tunneling as well as a closer look at semiconductor-metal contacts have been discussed. The basic function and importance of resonant tunneling diodes have been presented in the introduction sections. Furthermore, this work showed commonly used technology for fabrication of semiconductor heterostructures, especially for RTDs. Additionally, detailed fabrication recipes can be found in chapter 3 and the growth sheets of all fabricated RTDs are listed in appendix A. Finally, RTD measurements and results are presented and discussed in this chapter.

4.1 Basic Quantities

In this subchapter, the growth sheets for the sample R188 (13 nm well), R189 (10 nm well), R201 (20 nm well) and R207 (7nm well) are shown and furthermore, simulated bandstructures as well as simulated energy levels of the resonant states inside the quantum-well for all samples are presented in detail.

4.1.1 Growth Sheet

All fabricated RTDs consist of an $In_{0.53}Ga_{0.47}As$ quantum-well sandwiched by two $GaAs_{0.51}$-$Sb_{0.49}$ barriers. As shown in Tab.4.1, the samples only differ by variation of the quantum-well width. All of the other layers, especially barrier height and thickness, are the same for each sample. The width of each barrier is 9 nm and the conduction band offset between $In_xGa_{1-x}As$ and $GaAs_xSb_{1-x}$ is approximately 360 meV as already described in more detail in chapter 2. Due to the thin barrier thickness, tunneling effects can be observed.

The dopant gradient, as mentioned in chapter 2 and also seen in Tab.4.1, ensures good ohmic contacts and a smooth conduction band profile on both sides of the heterostructure. Together with ohmic metal contacts, it is possible to minimize unwanted effects influencing the I-V curves of the measured RTDs. All InGaAs and GaAsSb layers have a thickness between 9 nm and 500 nm with exception of the InP:Fe substrate (SI), which is approximately 350 µm thick. As mentioned before, only the quantum-well thickness was varied for each sample. Therefore, to analyse the RTD behaviour of different quantum-well widths, the thickness was systematically increased, starting from 7 nm for sample R201, 10 nm for R189, 13 for R188 to 20 nm for R207.

Layer	Thickness(nm)	Doping (1/cm^3)
Substrate	350 um	SI
InGaAs	500	2.00e18
InGaAs	100	2.00e17
InGaAs	100	2.00e16
InGaAs	50	
GaAsSb	9	
InGaAs	7 (R201) ; 10 (R189) ; 13 (R188) ; 20 (R207)	
GaAsSb	9	
InGaAs	50	
InGaAs	100	2.00e16
InGaAs	100	2.00e17
InGaAs	100	2.00e18

Table 4.1: Growth sheets of the RTD structures

4.1.2 Bandstructure

The displayed bandstructures of InGaAs/GaAsSb heterostructures were simulated with the programm *1D Poisson version beta 8g* written by Gregory Snider.[52] As mentioned before, the samples differ only in quantum-well thickness, which has only minor influence on the contact layers as long as all the other parameters are matching and the well width is only changed by a few nanometers for each sample. For the, later shown, simulation of the *quasi-bound energy states* inside the quantum-well, its thickness plays a vital role. It can be expected that with increasing thickness of the the quantum-well, the number of energy states is increasing too. For the basic bandstructure, only the sample R188, containing a 13 nm quantum-well and 9 nm barriers, was simulated, which can be seen at Fig.4.1. The stepwise gradation of the doping level on both sides of the double-barrier was done to allow a smooth band profile.

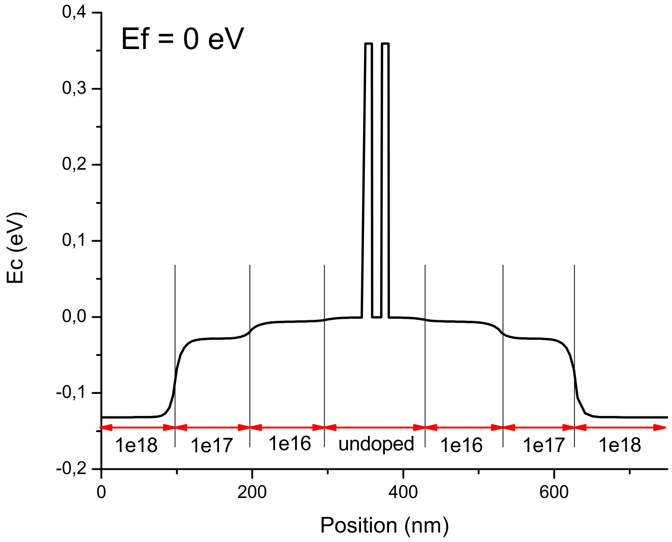

Figure 4.1: Simulated conduction band profile of the double-barrier heterostructure of sample R188.

Additionally, the electron density was simulated as shown in Fig.4.2. There should be no noticeable electron density for electronic barriers, which is also proven by the simulation. The lowest density should occur inside the quantum-well due to the short lifetime, as the electrons leave the well by tunneling through the barrier.

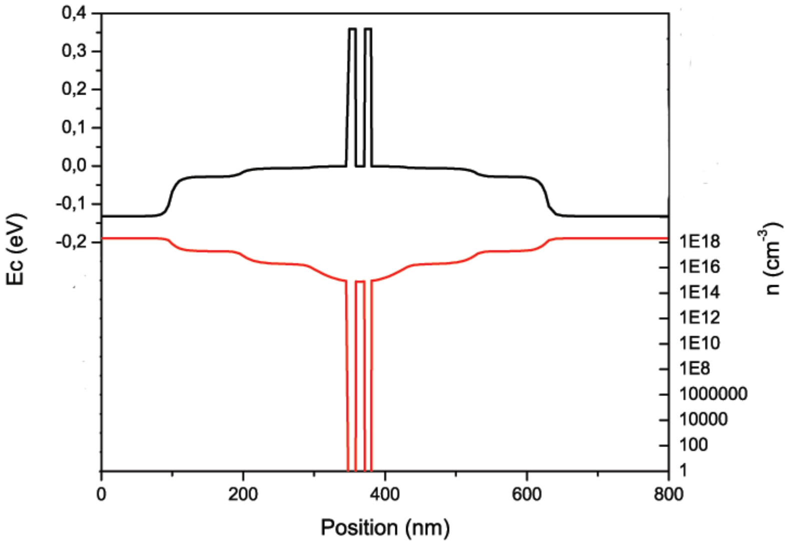

Figure 4.2: Simulated electron density (lower line) and conduction band structure (upper line) for sample R188 (13 nm well).

Due to the fermi energy difference of 0.1 eV, the bandstructure shown in Fig.4.1 bends, depending on the side, the fermi energy is changed. Furthermore, the energy difference between the conduction band edge on the left and right border of the simualtion corresponds directly to the difference of the fermi energies in the contact regions. This is shown in Fig.4.3.

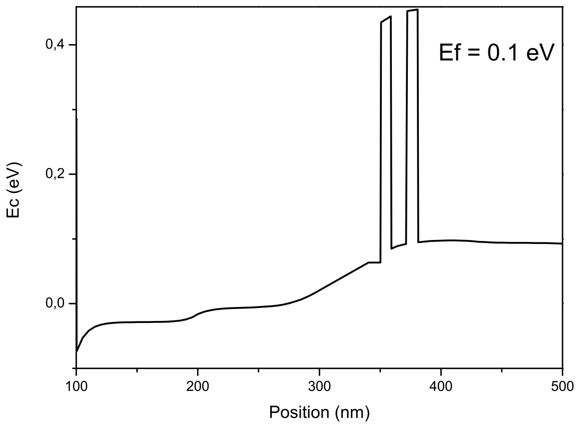

Figure 4.3: Simulated conduction band profile of sample R188 (13 nm well) for a fermi energy difference of 0.1 eV.

Finally, the energy-levels inside the double-barrier structure have been simulated for sample R188 using a Schrödinger solver within the envelope function approximation.[13] This is shown in Fig.4.4. Theoretically, the so-called *resonant states* should drift depending on the thickness of the quantum-well. As mentioned before, more *quasi-bound states* should appear with increasing quantum-well thickness. The four resonant states for the 13 nm quantum-well sample can be found at 35.5 meV for the first state, at 123.7 meV for the second state, at 236,4 meV for the third state and at 349 meV for the fourth state. The resonant state energies are also shown in Tab.4.2 together with the energies of the resonant states for the samples R189, R201 and R207.

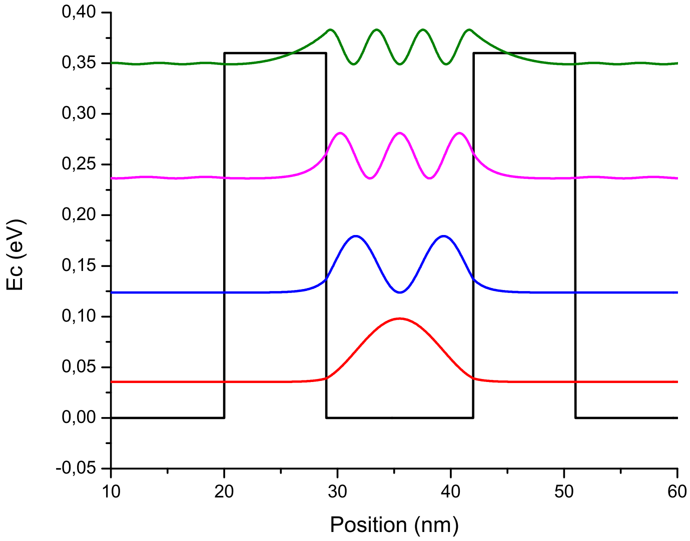

Figure 4.4: Simulated resonant states inside the 13 nm quantum-well (R188).

Sample	E_1 (meV)	E_2 (meV)	E_3 (meV)	E_4 (meV)	E_5 (meV)	ΔE_{12} (meV)
R207 (20 nm well)	17,2	64,1	131	209,1	291,5	46,9
R188 (13 nm well)	35,5	123,7	236,4	349	x	88,2
R189 (10 nm well)	53,3	175,4	311,7	x	x	122,1
R201 (7 nm well)	87,2	260,1	x	x	x	172,9

Table 4.2: Resonant state energy levels for the samples R188 (13 nm well), R189 (10 nm well), R201 (7 nm well) and R207 (20 nm well). ΔE_{12} is defined as energy difference between the energy of the second resonant state and the energy of the first resonance state.

4.2 Current-Voltage Characteristics

The I-V characterisations, presented in the following, were measured by using the HP Parameter Analyser at temperatures of 78 K and 300 K. Furthermore, all measured samples were shielded from light. To achieve accurate I-V characteristics of resonant tunneling diodes, it is necessary to eliminate as many parasitic effects as possible. One of the most important one are not perfectly ohmic contacts, which lead to asymmetric behaviour of the RTD. In reality, perfect ohmic contacts can not be achieved, but good approximations with a small Schottky-barrier impact are reached. This was already discussed in chapter 2 as well as other parasitic effects, which should be reduced as much as possible during the fabrication process. Furthermore, to acquire symmetric behaviour, it should be considered to embed interface engineering to improve symmetric behaviour of the resonances and NDR, which will be further discussed in the chapter *Outlook*. Selected I-V curves from samples with different quantum-well widths and RTD sizes are shown in this subchapter to explain important characteristics in more detail. Above the second resonance, the current density is comparable for all measured RTDs.

I-V characteristics of sample R188 (13 nm well)

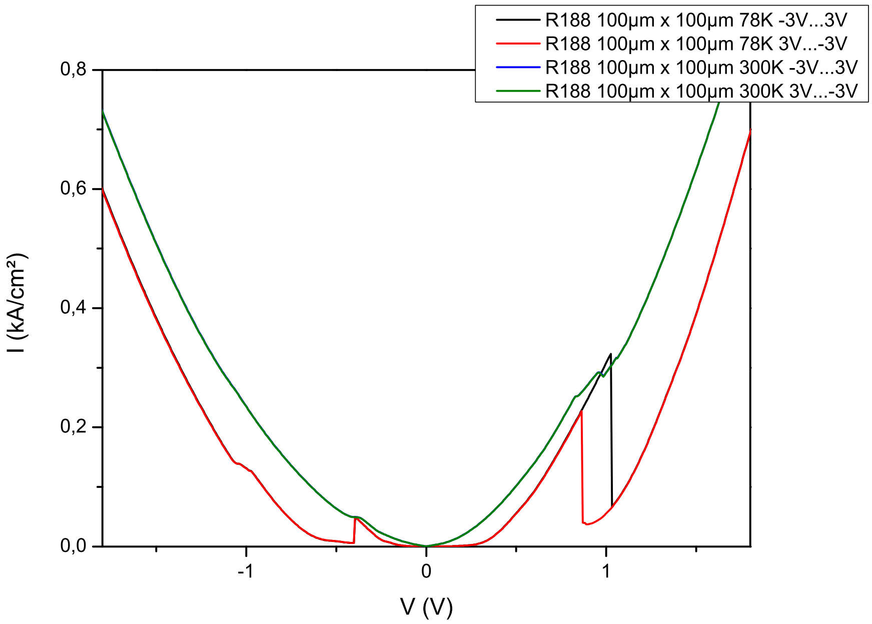

Figure 4.5: Linear I-V characterisation for the 100µm x 100µm RTD at 78K and 300 K (R188).

In Fig.4.5, the I-V characterisation for the 100µm x 100µm RTD is plotted. To show the temperature depending PVRs, I-V curves at 78 K and 300 K are compared. At 300 K, no first resonance is observed for both voltage sweep directions. The second resonance occurs at 0,96 V for the positive voltage range and at -0,36 V for the negative voltage range. The PVRs at 300 K are rather small due to temperature induced scattering. At 78 K, again no first resonance can be seen, but a much higher PVR of 4,8 is seen for the second resonance for the positive voltage range, compared to the PVR of 1,01 at 300 K. The difference of the PVRs is given by a factor of 4,8. Additionally, a considerable shift of the second resonance towards higher voltages is observed between the voltage sweeps from -3 V to 3 V (resonance occurs at 1,026 V) and in the opposite direction from 3 V to -3 V (resonance occurs at 0,864 V). This voltage shift of 0,162 V is associated to charging effects inside of the quantum-well depending on the voltage sweep direction. Theoretically, due to the symmetric design of the RTD, the resonances should occur at the same voltage for both voltage sweep direction. Nonetheless, the measured resonances differ in occurring voltage for the negative voltage range, respectively positive voltage range.

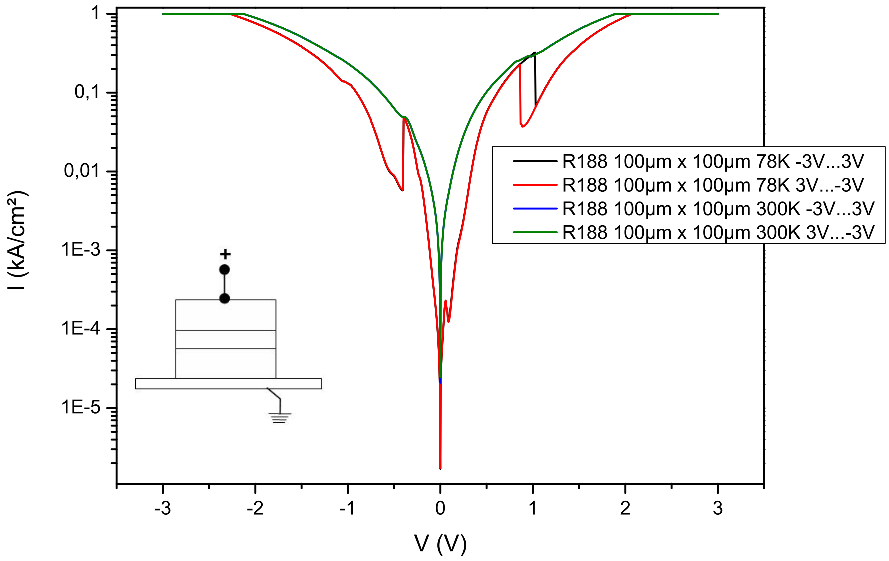

Figure 4.6: Logarithmic I-V characterisation for the 100µm x 100µm RTD at 78 K and 300 K (R188). As seen by the inset, positive voltage always denotes "+" on top of the mesa structure.

By using a logarithmic scale as shown in Fig.4.6 instead of a linear one (see Fig.4.5), the not visible first resonance at linear scaling is now observable at 78 K for the positive voltage range at 0,06 V with a PVR of 1,87, but not seen at 300 K at all. Conclusively, at 300 K, the first resonance is simply washed out due to the already mentioned temperature induced scattering. In summary, for lower temperatures, the NDR and the PVR increases. For positive voltage range, the second resonance consists of a PVR of 4,86.

I-V characteristics of sample R188 PR (13 nm well) ; processed without SiN

To study, if the used SiN isolation layer has any influence on the I-V-characteristics due to induced strain on the material, sample R188 PR was fabricated without a SiN isolation layer. Instead only photoresist was used for the fabrication.

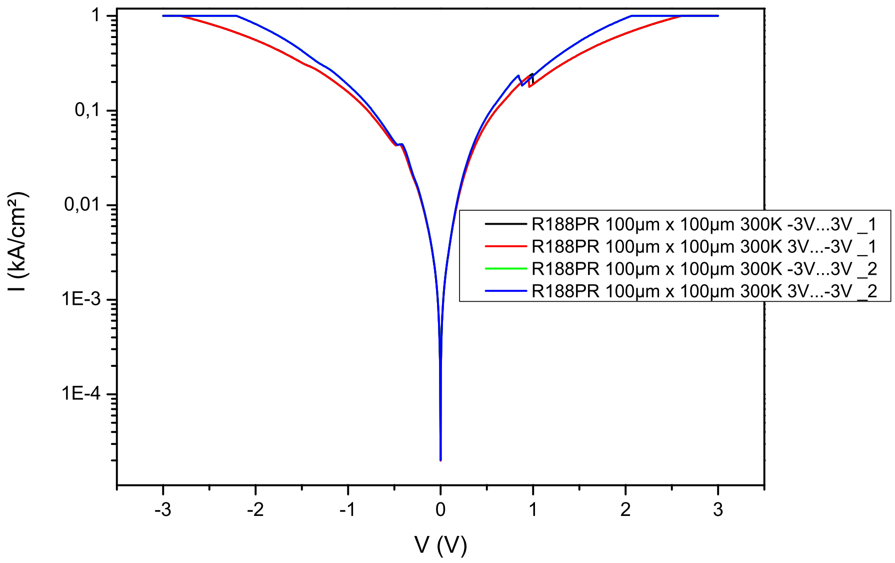

Figure 4.7: I-V characterisation for the 100µm x 100µm RTD at 300 K (R188PR) processed without SiN isolation layers.

Furthermore, the I-V curves of two different RTDs from sample R188 PR are compared to show, that there is often a small voltage shift of occurring resonances between different RTDs of the same sample. As well as for sample R188, the first resonance of sample R188PR 100µm x 100µm at 300 K is again washed out and the second resonance shows only very small PVR at room-temperature, which can be observed in Fig.4.7 at the voltages of 0,99 V for the first RTD and at 0,84 V for the second RTD for the positive voltage range and for both RTDs at -0,414 V for the negative voltage range. The mismatch of 0,15 V between the two resonances of the two RTDs for positive voltage range can be explained by additional serial resistances, caused by an increasing distance between the bond pad[1] and the device.

---

[1] Circuit points of the "*Dual In-Line (DIL)*"-casing to provide a low impedance connection to the devices.

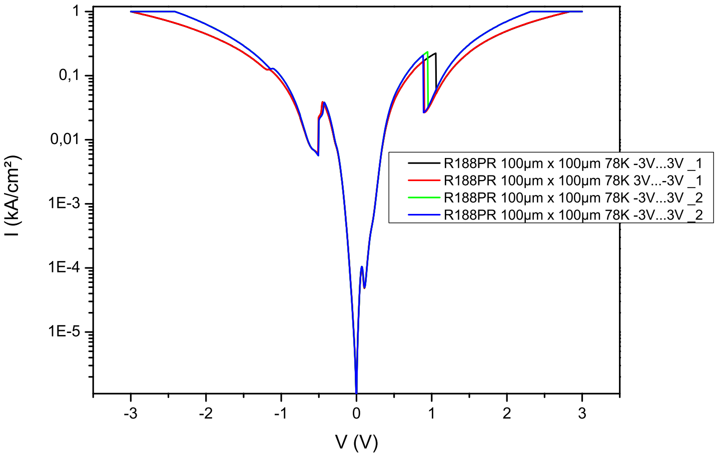

Figure 4.8: I-V characterisation for the 100µm x 100µm RTD at 78 K (R188PR).

Additionally, the same two RTDs shown in Fig.4.7 at 300 K are measured also at 78 K. The low temperature I-Vs of these samples are shown in Fig.4.8. Again it is observed that for lower temperatures, the PVRs are more pronounced. Additionally, as for the sample R188, the first resonance for the positive voltage range is seen. The actual difference between the PVRs of the first and second resonances of the samples R188 and R188 PR are shown in Tab.4.5.

PVR	R188 (SiN isolation)	R188 PR (no SiN isolation)	Δ PVR
First resonance	1,87	2,02	0,38
Second resonance	4,86	6,44	1,57

Table 4.3: The actual difference between the PVRs of the first and second resonances of the samples R188 and R188 PR for the positive voltage range. The SiN isolation layer reduces the PVR at the first resonance by 0,38248 and at the second resonance by 1,5723.

At a first conclusion, the induced strain of the SiN isolation layer does not affect the positions of the occurring resonances, but reduces the PVR at the first resonance by 0,38248 and at the second resonance by 1,5723.

In summary, the combined I-V characterisation for the sample R188PR 100µm x 100µm is shown in Fig.4.9 for PVR comparison at 300 K and at 78 K. The first resonance at 300 K is washed out due to the high temperature, but the second resonance at 300 K occurs at the same voltage as the resonance at 78 K does, but due to the reduced scattering at 78 K, higher NDR and PVR is measured.

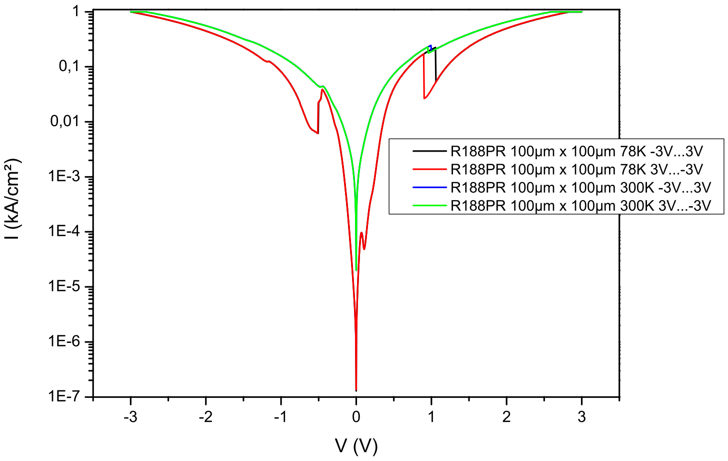

Figure 4.9: I-V characterisation for the 100µm x 100µm RTD at 300 K and at 78 K (R188PR).

I-V characteristics of sample R189 (10 nm well)

The 5µm x 5µm RTD was the smallest RTD size measured at the the experimental part of this thesis. The linear I-V characterisation is shown in Fig.4.10 at 78K for sample R189 (10 nm well).

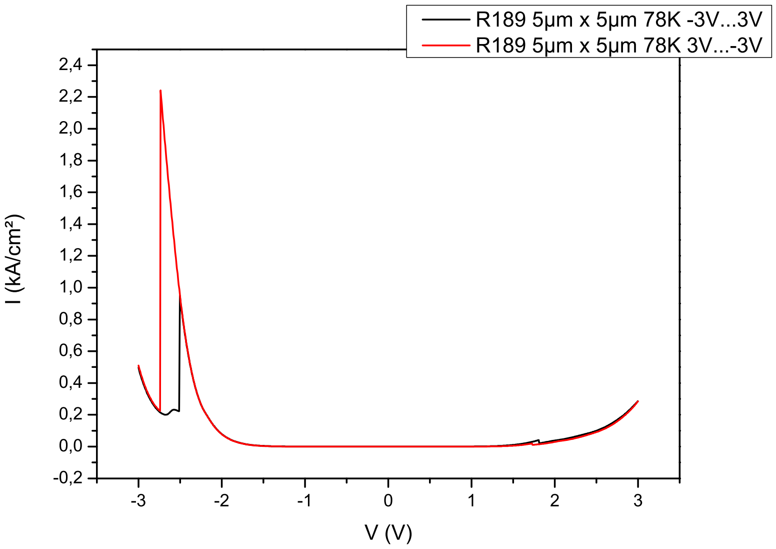

Figure 4.10: Linear I-V characterisation for the 5µm x 5µm RTD at 78 K (R189).

At linear scaling, no first resonances can be observed. The second resonances differ massively between the positive voltage range and the negative voltage range. At positive voltage range, only a very small PVR of 2 occurring at the voltage of 1,8 V, while at negative voltage range, a PVR of 4,26 for positive voltage sweep and an even higher PVR of 9,99 for a negative voltage sweep. Additionally the voltage of the second resonances for positive voltage sweep and the negative voltages sweep changes from -2,5 V for the positive sweep to -2,73 V for the negative sweep.

By changing to a logarithmic scaling, shown in Fig.4.11, only the first resonance for the positive voltage range is observed at 0,26 V and contains a PVR of 1,44. No first resonance for negative voltage range is observed. The sample could not be driven beyond the range of -3 V to 3 V for further studies without extended damage to the heterostructure. Therefore, all measurements had to be within this voltage range.

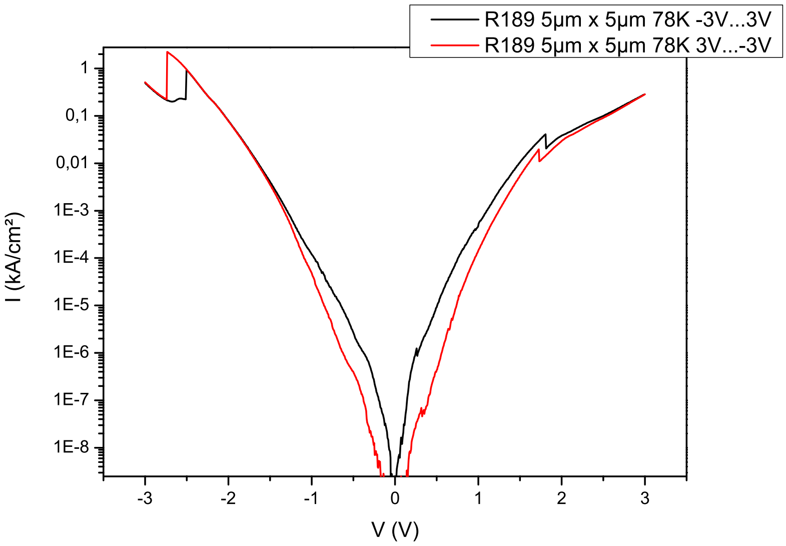

Figure 4.11: Logarithmic I-V characterisation for the 5µm x 5µm RTD at 78 K (R189).

I-V characteristics of sample R207 (20 nm well)

Sample R207 consist of a 20 nm quantum-well. The thicker the quantum-well is, the more resonant energy states are contained inside. This is shown in Fig.4.12 which displays the I-V characterisation at 78 K for sample R207 100µm x 100µm. Three resonances are seen, instead of only two resonances observed for all the other samples.

This agrees with the increased number of quasi-bound states of the calculation, shown in subchapter *bandstructure*. Nonetheless the simulated values for the energy levels do not exactly match the measured energy levels due to the necessary simplification of complex quantum-mechanical effects. But for a first estimation about resonant energy levels occurring inside the quantum-well, the simulation shows good results. The voltages associated to the

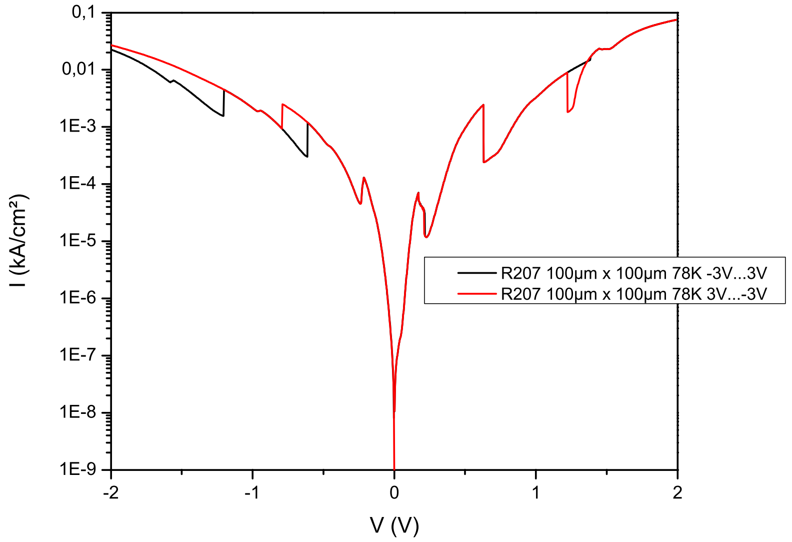

Figure 4.12: I-V characterisation for the 100µm x 100µm RTD at 78 K (R207).

measured resonances are listed in Tab.4.4 for 100µm x 100µm RTDs of the samples R207 (20 nm well), R188 (13 nm well), R189 (10 nm well), R201 (7 nm well) at 78 K. P_{1+}, P_{2+} and P_{3+} are associated to the first resonance, the second resonance and the third resonance for the positive voltage range. The energies of the resonant states inside the well depend on the thickness of the well. As shown in the simulation, for increasing well thickness, the energy level of the first resonance decreases and more resonant states are coming into existence. This trend can also be seen for resonances of the measured RTDs of the samples R207 (20 nm well), R188 (13 nm well), R189 (10 nm well), R201 (7 nm well) at 78 K.

Sample	P_{1+}	P_{2+}	P_{3+}
R207 (20 nm well)	x	170 mV	630 mV
R188 (13 nm well)	60 mV	x	1,026 V
R189 (10 nm well)	115 mV	x	x
R201 (7 nm well)	355 mV	x	x

Table 4.4: The voltages associated to the measured resonances are listed for 100µm x 100µm RTDs of the samples R207 (20 nm well), R188 (13 nm well), R189 (10 nm well), R201 (7 nm well) at 78 K. P_{1+}, P_{2+} and P_{3+} are associated to the first, the second resonance and the third resonance for the positive voltage range. A trend can be seen, that the energy level of the first resonance is decreasing with the thickness of the quantum-well.

4.3 Peak-to-Valley Ratio versus RTD size

One part of this thesis was to characterize the behaviour of the voltage-current curves for different RTD sizes. Therefore, 100µm x 100µm, 40µm x 40µm, 30µm x 30µm, 10µm x 10µm and 5µm x 5µm RTDs have been processed. The idea was that by reduction of the actual RTD size, an increase of the peak-to-valley ratio for the device should be measurable. This is directly associated to the surface defects occurring during the growth of the heterostructure. Due to reduced RTD size, the number of surface defects, which negatively influence the RTD behaviour, should be largely reduced or even avoided. Therefore a higher PVR is expected. In a first study, measurements were done for device geometries of 40µm x 40µm, 10µm x 10µm and 5µm x 5µm.[2] The tendency towards larger PVRs for smaller devices, shown in Fig.4.13, is clearly visible.

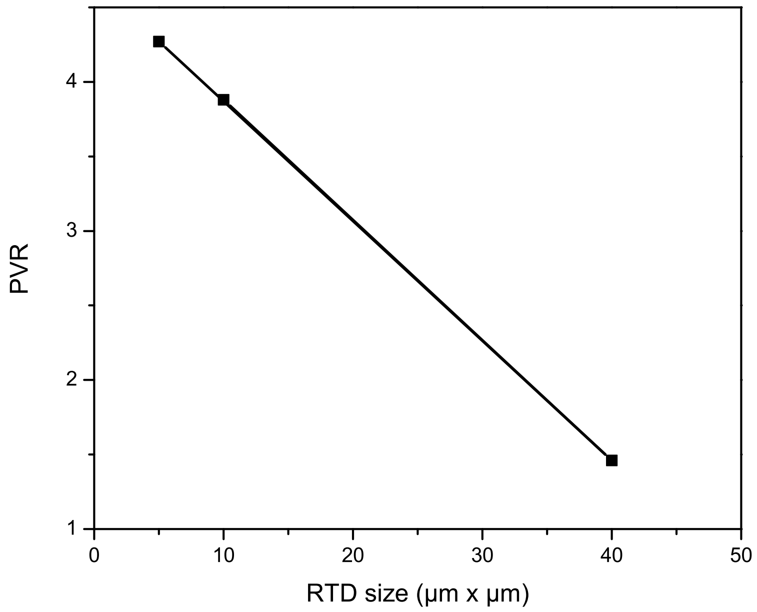

Figure 4.13: Peak-to-valley ratios of sample R189 for quantum-well widths of 40µm x 40µm, 10µm x 10µm and 5µm x 5µm, measured at 78 K. A PVR of 1,46 was measured for the 40µm x 40µm RTD, a PVR of 3,88 for the 10µm x 10µm RTD and a PVR of 4,27 for the 5µm x 5µm RTD. The smaller the actual size of the RTD, the higher the PVR becomes. [53]

As shown in Tab.4.5 a PVR of 1,46 was measured for the 40µm x 40µm RTD, a PVR of 3,88 for the 10µm x 10µm RTD and a PVR of 4,27 for the 5µm x 5µm RTD. Therefore, the

---

[2] Due to a different processing of large mesas (100µm x 100µm), a direct comparison of small to large mesas can not be given.

PVR between the 40µm x 40µm RTD and the 10µm x 10µm RTD by is increased by factor 2,65. Furthermore, comparison of the 40µm x 40µm RTD and the 5µm x 5µm RTD shows even a further increase by factor 2,92.

R189 (10 nm well)	PVR	PVR increase by factor (based on the 40µm x 40µm RTD)
40µm x 40µm	1,46	x
10µm x 10µm	3,88	2,65
5µm x 5µm	4,27	2,92

Table 4.5: PVRs for 40µm x 40µm RTDs, 10µm x 10µm RTDs and 5µm x 5µm RTDs of sample R189 (10 nm well). PVRs between the different RTD sizes shows an increase by a factor of 2,65753 for the 10µm x 10µm RTD compared to the 40µm x 40µm RTD. Further reduction of the RTD size from 40µm x 40µm down to the 5µm x 5µm shows again an increase by the factor of 2,92.

Due to the restricted time of this diploma thesis and general difficulties, when processing such small structures with conventional lithography techniques, the amount of available data was limited. Nevertheless, for the shown result, it can be observed, that there is an increase of the PVR value for smaller RTD sizes. This seems to prove that smaller RTD size has great influence on I-V curves and as a result on the PVR.

4.4 Interface Induced Asymmetry Effect

During this thesis, an effect has been observed that the I-V curve is slightly different depending on the direction, the current is passing through the structure. As sketched in Fig.4.14, current passing from left to right shows different I-V characteristics than current passing from right to left. Further research was done to analyse this phenomenon by using RTDs with the result, that the growth direction of the heterostructure seems to have direct influence to the I-V characterisation for different current directions. One possible explanation for this connection is the interface roughness at the interfaces between the layers during the growth inside the molecular beam epitaxy chamber. It is assumed that the interface roughness between the InGaAs layer and the GaAsSb layer is only minor, but a non-negligible interface roughness between the GaAsSb and InGaAs is occurring. In Fig.4.14, a schematic of the expected interface roughness difference is shown.

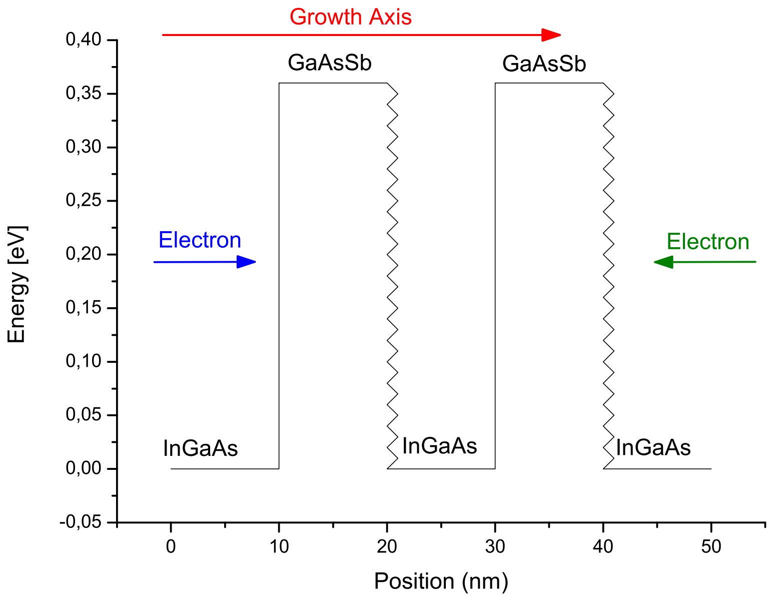

Figure 4.14: Schematic of occurring interface roughness during MBE growth. Interface roughness between the InGaAs layer and the GaAsSb layer is only minor, but a non-negligible interface roughness between the GaAsSb and InGaAs is occurring. Therefore, electrons encounter interfaces of different roughness depending on the tunneling direction.

Under consideration of this fact, the results of measured RTD I-V curves were further studied and combined characteristics can be seen at Fig.4.15. Samples of different well width are shown and the position and symmetries of occurring resonances are compared.

At a first conclusion, it seems that there is an association between the thickness of the quantum-well and the quality of the interface. The interface quality of thicker quantum-wells seems to differ from the interface quality of thinner quantum-wells. This might correspond directly to the lower or higher interface roughness[3]. This higher interface roughness can be witnessed as larger voltage offset for occurring resonances. This result is further proven by similar behaviour of symmetric quantum-cascade lasers also fabricated at the Vienna University of Technology. This theory is still preliminary due to the small amount of data achieved during the time frame of this thesis. Further investigations have to be done to proof the connection between interface roughness and the asymmetries of the I-V behaviour. Nonetheless, this result raises the question, if interface engineering could lead to a considerable performance enhancement.

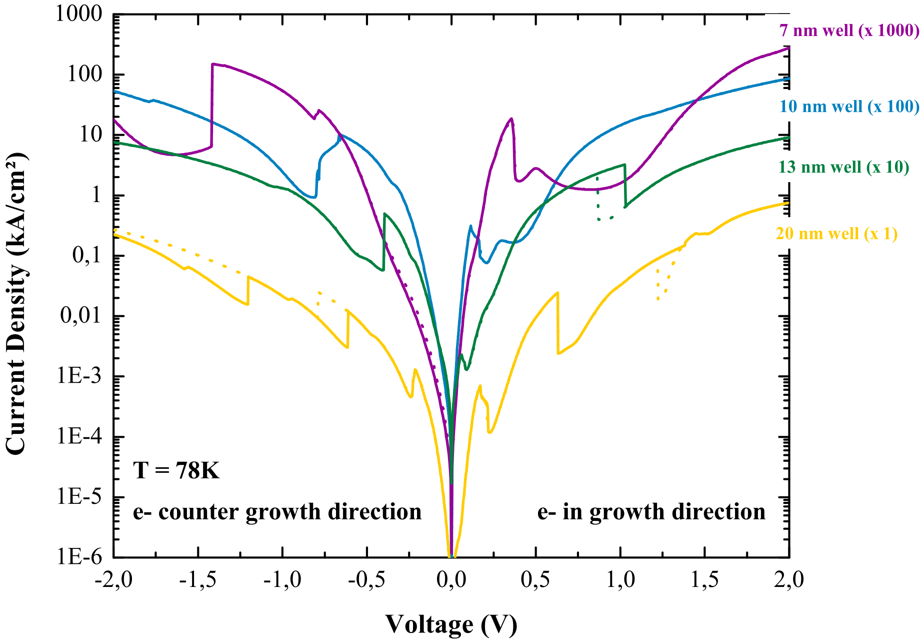

Figure 4.15: I-V characteristics for symmetrical RTD's containing different quantum-well sizes at 78 K. Asymmetrical behaviour can be observed depending on growth direction.[53]

Additionally, PVR measurements for different quantum-wells revealed an interesting result, shown in Fig.4.16. These data indicate, that the PVR is increasing for decreasing quantum-well widths, if the current direction matches the growth direction (InGaAs / GaAsSb interface). The comparison of the PVR of 20 nm well width and 7 nm well width indicates even an increase by a factor of 5. For the case that the current direction is opposite to the growth direction (GaAsSb / InGaAs interface), PVRs seem to be scattered and no trend can be observed.

---

[3] The influence of the interface roughness decreases the thicker a well is, thus it is important to minimize the interface roughness for thin wells.

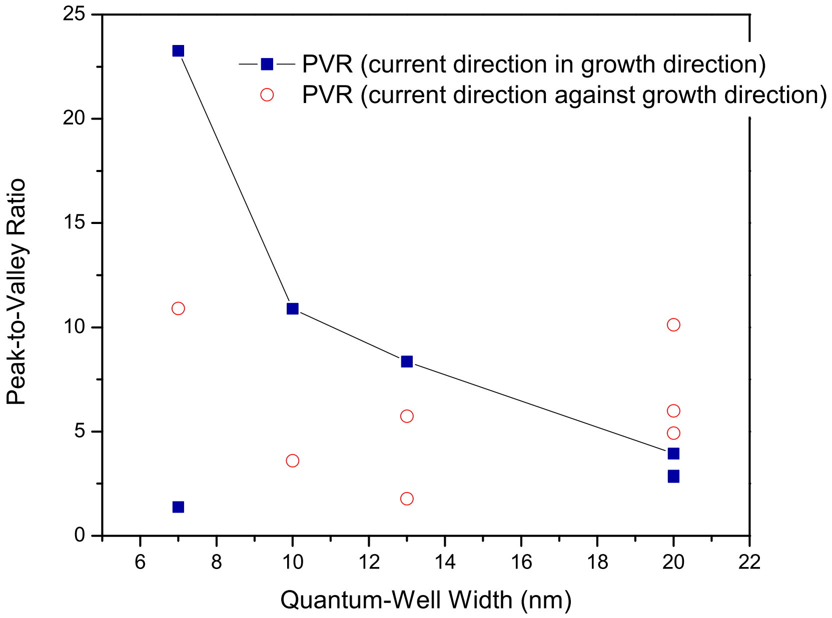

Figure 4.16: Peak-to-valley ratio of RTDs of different quantum-well thickness. The blue squares represent the measured peak-to-valley ratios for each well thickness for current direction equals to growth direction (InGaAs / GaAsSb interface). The highest measured PVR were connected by a line to show the trend of higher PVR for smaller quantum-well widths. The red open circles correspond to peak-to-valley ratios for each well thickness for current direction against the growth direction (GaAsSb / InGaAs interface). The PVRs seem to be scattered and so far no trend can be observed.[53]

4.5 Magnetic Effects on the $In_xGa_{1-x}As/GaAs_xSb_{1-x}$ Material System

Research on the behaviour of InGaAs/GaAsSb RTDs under the influence of magnetic fields has been already started by Silvano de Sousa, Jürgen Smoliner *et al.* at the Institute of Solid-State Electronics at the Vienna University of Technology. First results were already published about non-parabolic effects by analysing results from magneto-tunneling experiments. In this publication, [54], it was shown that electron masses on samples with high resonance energies and small well widths are rising rapidly due to the nonparabolic bandstructures. An interesting observation has been made, that with increasing Landau levels index the effective electron mass is decreasing, which can be explained by the quantum confined Stark effect. This decrease in effective mass can be seen in Fig.4.17.

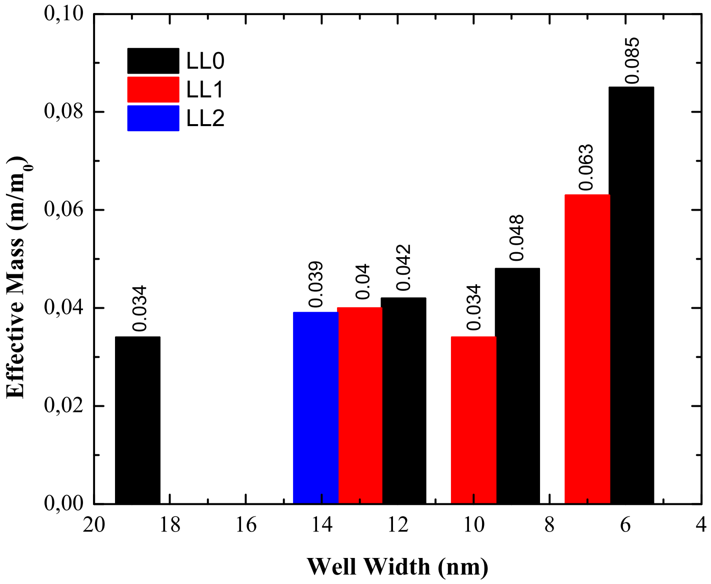

Figure 4.17: To each quantum-well width of 7 nm, 10 nm, 13 nm and 20 nm, a group of columns (each column corresponds to a Landau level respectively to the effective mass) is associated. Slightly modified from [54].

Due to RTDs, fabricated during the experimental part of this diploma thesis, further investigation was done to enhance the understanding of the magnetic field influence and non-parabolicity effects on the InGaAs/GaAsSb material system. Due to this research, possible large spin splitting effects were observed for a wide range of temperatures. Furthermore, at magnetic fields of 5 Tesla, a PVR of 2.5 has been witnessed and split peak values of a maximum of 30 meV have been measured. This splitting is highly temperature insensitive and is occurring up to 180 K and additionally associated with the quantum-well width of the RTD. This resonance peak splitting might be associated to a large effective g factor in the case of a *Zeeman splitting* model. Nonetheless, there is also the possibility to fit this phenomenon in terms of Rashba effect. The best theoretical approach to these possibly spin related effects in this material system are still underway. This research was again done leading by Silvano de Sousa, Jürgen Smoliner *et al.* at the Institute of Solid-State Electronics at the Vienna University of Technology. Achieved results are not yet published, but are under intensive development and will soon be released. However first results of the described resonance peak splitting phenomenon can be observed at Fig.4.18.

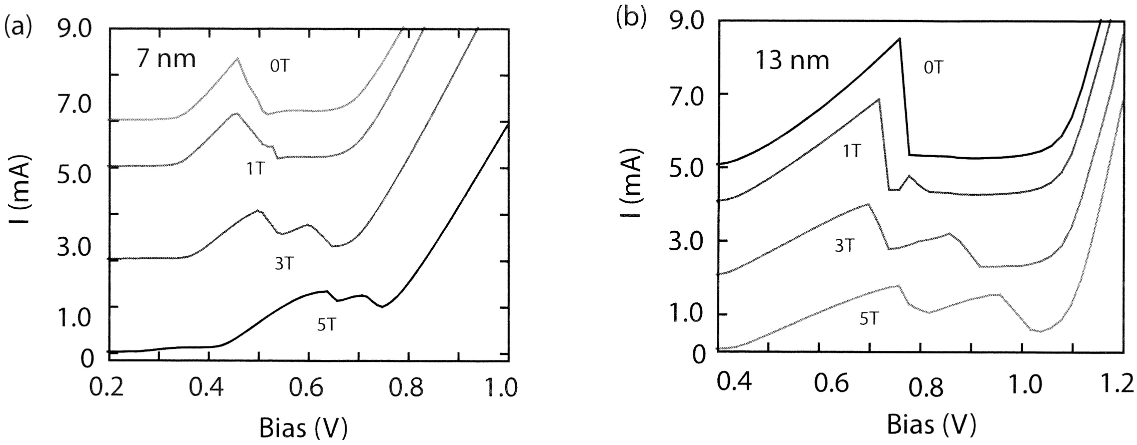

(a) Sample with a quantum-well of 7 nm.

(b) Sample with a quantum-well of 13 nm.

Figure 4.18: I-V characteristic at a magnetic field of 0 T, 1 T, 3 T and 5 T at a temperature of 4.2 K for a quantum-well of 7 nm (a) and 13 nm (b). The splitting effect is getting stronger with increasing magnetic fields.[55]

Chapter 5

Summary

Technology advancement in growth techniques and the motivation to improve the performance of semiconductor devices is a strong motivation to test and research new material systems. Furthermore, efforts are made to replace aluminum containing materials for different reasons, like the disadvantage of higher electron mass and difficulties during the MBE growth with GaAs, like increased surface roughness, explained in chapter 1. Such a material compound is the InGaAs/GaAsSb heterostructure which is additionally lattice matched to a InP substrate. The purpose of this work was to characterize and analyse this material system by usage of resonant tunneling diodes. RTDs were used for research and analysing, because they provide good information about electron transport and quantum-mechanical effects in semiconductor heterostructures even up to room-temperature. Two different lithography mask designs were used to fabricate RTDs of different sizes from 100µm x 100µm down to 5µm x 5µm. Detailed recipes for fabrication of the different RTD designs were thoroughly planned and tested. The resulting recipes are presented in this work and allow future re-fabrication and modifications. Additionally, the different designs contain slightly different quantum-well thickness to study the influence on the I-V characteristics. Furthermore, the peak-to-valley ratio was examined for all of the samples and first results lead to the conclusion, that RTD size does directly influence the PVR. This could be a direct result of reducing or avoiding surface impurities. Furthermore, an interesting association between the thickness of the quantum-well and the roughness of the interface between the InGaAs and GaAsSb layers has been found. Further analyses shows a connection between the quality of the interface and the actual thickness of the quantum-well as well as growth direction influence on I-V characteristics. Further studies could lead to precisely done interface engineering to improve performance for not only RTDs, but furthermore for quantum-cascade lasers.

Chapter 6

Outlook

Many interesting applications and approaches could be done further on with the achieved results of this thesis. First of all, the approach in reducing actual RTD sizes, fabricated down to 5µm x 5µm in this thesis, should be continued, maybe even into the nanometer region. This would afford switching from optical lithography to other lithography techniques like automated *electron beam writing* fabrication. Also it is necessary to redraw or modify the already existing processing masks to take the differences in creating such small structures into account. Another approach could be by usage of other materials for insulating layers instead of silicone nitride. Zirconium oxide or polymeric materials should be taken into consideration. Research of the implementation of these materials has already started for the fabrication of other devices like quantum-cascade lasers at the Technical University of Vienna.

One more interesting approach to achieve a better symmetric behaviour of I-V characteristics as well as reduce interface roughness is *interface engineering*. Introducing interface engineering into the growth process is no easy task and extends growth time by far, but would quite possible lead to an improvement of semiconductor device performance. This was not considered for the processed RTD's during this thesis, but could lead in the future to considerably advancement in RTD symmetric resonance and NDR behaviour. This would also allow to better reproduce I-V curves, which is still a problem for state-of-the-art RTD's, not only for InGaAS/GaAsSb material systems, but for mostly all of them. The RTD as testing devices is pre-destinated to calibrate interface engineering done for the growth as well as to analyse and intepret the results and their impact on other semiconductor devices like the quantum-cascade laser or the QWIP.

Last, but not least, there is also the interesting idea of expanding the basic RTD behaviour of only considering electron transport to electron and hole transport. This is called *Resonant Interband Tunneling Diode (RIT)*.[12]

Appendix A

Growth Sheets

Layer	Thickness(nm)	Doping (1/cm^3)
Substrate	350 um	SI
InGaAs	500	2.00e18
InGaAs	100	2.00e17
InGaAs	100	2.00e16
InGaAs	50	
GaAsSb	9	
InGaAs	13	
GaAsSb	9	
InGaAs	50	
InGaAs	100	2.00e16
InGaAs	100	2.00e17
InGaAs	100	2.00e18

Table A.1: Growth Sheet of R188

Layer	Thickness(nm)	Doping (1/cm^3)
Substrate	350 um	< 4.00e17
InGaAs	500	2.00e18
InGaAs	100	2.00e17
InGaAs	100	2.00e16
InGaAs	50	
GaAsSb	9	
InGaAs	10	
GaAsSb	9	
InGaAs	50	
InGaAs	100	2.00e16
InGaAs	100	2.00e17
InGaAs	100	2.00e18

Figure A.1: Growth Sheet of R189

Layer	Thickness(nm)	Doping (1/cm^3)
Substrate	350 um	SI
InGaAs	500	2.00e18
InGaAs	100	2.00e17
InGaAs	100	2.00e16
InGaAs	50	
GaAsSb	9	
InGaAs	7	
GaAsSb	9	
InGaAs	50	
InGaAs	100	2.00e16
InGaAs	100	2.00e17
InGaAs	100	2.00e18

Figure A.2: Growth Sheet of R201

Layer	Thickness(nm)	Doping (1/cm^3)
Substrate	350 um	SI
InGaAs	500	2.00e18
InGaAs	100	2.00e17
InGaAs	100	2.00e16
InGaAs	50	
GaAsSb	9	
InGaAs	20	
GaAsSb	9	
InGaAs	50	
InGaAs	100	2.00e16
InGaAs	100	2.00e17
InGaAs	100	2.00e18

Table A.2: Growth Sheet of R207

List of Figures

1.1 Lattice constants for a variety of materials.[10] 10

2.1 Lattice constants for a variety of materials.[18] 14
2.2 Bandstructure of $In_xGa_{1-x}As$.[18] 15
2.3 Bandstructures of GaAs and GaSb.[18] 16
2.4 Bandstructure of the conduction band and the valence band of InGaAs/GaAsSb. The conduction band offset between $In_{0.53}Ga_{0.47}As$ and $GaAs_{0.51}Sb_{0.49}$ is 0.36 eV.[9] 17
2.5 Tunneling through a potential barrier for electron energy lower than the energy of the barrier.[12] 18
2.6 The wavefunction is decreasing exponentially inside of a finite barrier.[30] . . 20
2.7 Correlation between the transfer matrix coefficients.[12] 21
2.8 Transmission coefficient for a single-barrier structure.[12] 25
2.9 Asymmetric single-barrier structure.[12] 26
2.10 InGaAs/GaAsSb double-barrier structure 27
2.11 Correlation between the transfer matrix coefficients for a symmetric double-barrier structure.[12] 28
2.12 Asymmetric double-barrier structure.[12] 30
2.13 Schottky contact and ohmic contact energy band diagram and I-V of a ohmic contact.[31] 33
2.14 Schematic of a InGaAs/GaAsSb RTD. Taken and modified from[33] 35
2.15 Bandstructure of a RTD with applied bias of changing value.[11] 36
2.16 Peak-to-valley ratio of a resonant tunneling diode. 37

3.1 Schematic of a typical molecular beam epitaxy growth chamber.[36] 40
3.2 Schematic of a RHEED monitoring technique.[38] 41
3.3 Chemical reaction during a PECVD process. 42
3.4 Function chart of a PECVD chamber.[40] 43
3.5 Different lithography technologies.[41] 44
3.6 Reactive ion etching chamber and working principle.[43],[44] 45

3.7 Behavior difference between dry-etching and wet-etching.[43],[44] 46
3.8 Endpoint detection of a SiN passivation layer.[46] 46
3.9 Schematic of a evaporation chamber.[46] 47
3.10 Process steps of the Lift-Off process.[48] 48
3.11 Schematic of a sputtering system.[49] 49
3.12 Sputter yield Y for different target materials and the dependence of the ion energy of 400 eV.[50] 49
3.13 Comparison of different deposition technologies.[45] 50
3.14 Fabrication mask for *Processing 1* and scheme of fabricated RTD. 52
3.15 Fabrication mask for *Processing 2* and image of fabricated RTD.[51] 55
3.16 Trends for different mixing ratios of the photo-resist AZ 5214 associated to variations of the spin velocity. 56

4.1 Simulated conduction band profile of the double-barrier heterostructure of sample R188. 61
4.2 Simulated electron density (lower line) and conduction band structure (upper line) for sample R188 (13 nm well). 62
4.3 Simulated conduction band profile of sample R188 (13 nm well) for a fermi energy difference of 0.1 eV. 62
4.4 Simulated resonant states inside the 13 nm quantum-well (R188). 63
4.5 Linear I-V characterisation for the 100µm x 100µm RTD at 78K and 300 K (R188). 64
4.6 Logarithmic I-V characterisation for the 100µm x 100µm RTD at 78 K and 300 K (R188). As seen by the inset, positive voltage always denotes "+" on top of the mesa structure. 65
4.7 I-V characterisation for the 100µm x 100µm RTD at 300 K (R188PR) processed without SiN isolation layers. 66
4.8 I-V characterisation for the 100µm x 100µm RTD at 78 K (R188PR). 67
4.9 I-V characterisation for the 100µm x 100µm RTD at 300 K and at 78 K (R188PR). 68
4.10 Linear I-V characterisation for the 5µm x 5µm RTD at 78 K (R189). 68
4.11 Logarithmic I-V characterisation for the 5µm x 5µm RTD at 78 K (R189). . . 69
4.12 I-V characterisation for the 100µm x 100µm RTD at 78 K (R207). 70
4.13 Peak-to-valley ratios of sample R189 for quantum-well widths of 40µm x 40µm, 10µm x 10µm and 5µm x 5µm, measured at 78 K. A PVR of 1,46 was measured for the 40µm x 40µm RTD, a PVR of 3,88 for the 10µm x 10µm RTD and a PVR of 4,27 for the 5µm x 5µm RTD. The smaller the actual size of the RTD, the higher the PVR becomes. [53] 71

4.14 Schematic of occurring interface roughness during MBE growth. Interface roughness between the InGaAs layer and the GaAsSb layer is only minor, but a non-negligible interface roughness between the GaAsSb and InGaAs is occurring. Therefore, electrons encounter interfaces of different roughness depending on the tunneling direction. 73
4.15 I-V characteristics for symmetrical RTD's containing different quantum-well sizes at 78 K. Asymmetrical behaviour can be observed depending on growth direction.[53] 74
4.16 Peak-to-valley ratio of RTDs of different quantum-well thickness. The blue squares represent the measured peak-to-valley ratios for each well thickness for current direction equals to growth direction (InGaAs / GaAsSb interface). The highest measured PVR were connected by a line to show the trend of higher PVR for smaller quantum-well widths. The red open circles correspond to peak-to-valley ratios for each well thickness for current direction against the growth direction (GaAsSb / InGaAs interface). The PVRs seem to be scattered and so far no trend can be observed.[53] 75
4.17 To each quantum-well width of 7 nm, 10 nm, 13 nm and 20 nm, a group of columns (each column corresponds to a Landau level respectively to the effective mass) is associated. Slightly modified from [54]. 76
4.18 I-V characteristic at a magnetic field of 0 T, 1 T, 3 T and 5 T at a temperature of 4.2 K for a quantum-well of 7 nm (a) and 13 nm (b). The splitting effect is getting stronger with increasing magnetic fields.[55] 77

A.1 Growth Sheet of R189 84
A.2 Growth Sheet of R201 84

List of Tables

2.1 Characteristics of $\mathrm{In}_x\mathrm{Ga}_{1-x}\mathrm{As}$ . . . 15
2.2 Characteristics of $\mathrm{GaAs}_{1-x}\mathrm{Sb}_x$ . . . 16
2.3 Possible metal semiconductors material combinations for ohmic contacts.[31] 32

3.1 Thickness of the different resist mixtures of AZ5214 depending on the spin velocity. . . . 57

4.1 Growth sheets of the RTD structures . . . 60
4.2 Resonant state energy levels for the samples R188 (13 nm well), R189 (10 nm well), R201 (7 nm well) and R207 (20 nm well). $\Delta\mathrm{E}_{12}$ is defined as energy difference between the energy of the second resonant state and the energy of the first resonance state. . . . 63
4.3 The actual difference between the PVRs of the first and second resonances of the samples R188 and R188 PR for the positive voltage range. The SiN isolation layer reduces the PVR at the first resonance by 0,38248 and at the second resonance by 1,5723. . . . 67
4.4 The voltages associated to the measured resonances are listed for 100µm x 100µm RTDs of the samples R207 (20 nm well), R188 (13 nm well), R189 (10 nm well), R201 (7 nm well) at 78 K. P_{1+}, P_{2+} and P_{3+} are associated to the first, the second resonance and the third resonance for the positive voltage range. A trend can be seen, that the energy level of the first resonance is decreasing with the thickness of the quantum-well. . . . 70
4.5 PVRs for 40µm x 40µm RTDs, 10µm x 10µm RTDs and 5µm x 5µm RTDs of sample R189 (10 nm well). PVRs between the different RTD sizes shows an increase by a factor of 2,65753 for the 10µm x 10µm RTD compared to the 40µm x 40µm RTD. Further reduction of the RTD size from 40µm x 40µm down to the 5µm x 5µm shows again an increase by the factor of 2,92. . . . 72

A.1 Growth Sheet of R188 . . . 83
A.2 Growth Sheet of R207 . . . 84

Bibliography

[1] A. Y. Cho; J. R. Arthur. Molecular Beam Epitaxy. *Bell Laboratories, Murray Hill, New Jersey*, 1975.

[2] B. F. Levine; K. K. Choi; C. G. Bethea; J. Walker; R. J. Malik. New 10 m infrared detector using intersubband absorption in resonant tunneling GaAlAs superlattices. *Appl. Phys. Lett. 50, 1092*, 1987.

[3] J. Faist; F. Capasso; D. L. Sivco; C. Sirtori; A. L. H. and A. Y. Cho. Quantum Cascade Laser. *Science Journal Vol. 264 no. 5158 pp. 553-556*, 1994.

[4] R. Köhler; A. Tredicucci; F. Beltram; H. E. Beere; E. H. Linfield; A. G. Davies; D. A. Ritchie; R. C. Iotti; F. Rossi. Terahertz semiconductor-heterostructure laser. *Nature London 417, 156*, 2002.

[5] B. S. Li; A. Shen; W. O. Charles; Q. Zhang; M. C. Tamargo. Midinfrared intersubband absorption in wide band gap II-VI ZnxCd1xSe multiple quantum wells with metastable zincblende MgSe barriers. *Appl. Phys. Lett. 92, 261104*, 2008.

[6] K. J. Franz; W. O. Charles; A. Shen; A. J. Hoffman; M. C. Tamargo; C. Gmachl. ZnCdSe/ZnCdMgSe quantum cascade electroluminescence. *Appl. Phys. Lett. 92, 121105*, 2008.

[7] M. J. Kane; S. Millidge; M. T. Emeny; D. Lee; D. R. P. Guy; C. R. Whitehouse. *Intersubband Transitions in Quantum Wells*. New York, Plenum Press, 1992.

[8] J. Faist. Wallplug efficiency of quantum cascade lasers: Critical parameters and fundamental limits. *Appl. Phys. Lett. 90, 253512*, 2007.

[9] H. Detz; A.M. Andrews; M. Nobile : P. Klang; E. Mujagic; G. Hesser; W. Schrenk; F. Schäffler; G. Strasser. Intersubband optoelectronics in the InGaAs/GaAsSb material system. *J. Vac. Sci. Technol.*, 2010.

[10] Brian R. Bennett; Richard Magno; J. Brad Boos; Walter Kruppa; Mario G. Ancona. Antimonide-based compound semiconductors for electronic devices: A review. *Solid-State Electronics 49 (2005) 1875-1895*, 2005.

[11] H. Mizuta; T. Tanoue. *The Physics and Applications of Resonant Tunnelling Diodes*. Cambridge: Cambrigde University Press, 1995.

[12] D. K. Ferry; S. M. Goodnick. *Transport in Nanostructures*. Cambridge: Cambrigde University Press, 1997.

[13] M. Nobile; H. Detz; E. Mujagic; A.M. Andrews; P. Klang; W. Schrenk; G. Strasser. Midinfrared intersubband absorption in InGaAs/GaAsSb multiple quantum wells. *Appl. Phys. Lett. 95, 041102*, 2009.

[14] C. Deutsch; A. Benz; H. Detz; P. Klang; M. Nobile; A. M. Andrews; W. Schrenk; T. Kubis; P. Vogl; G. Strasser; K. Unterrainer. Terahertz quantum cascade lasers based on type II InGaAs/GaAsSb/InP. *Appl. Phys. Lett. 97, 261110*, 2010.

[15] T. C. L. G. Sollner; W. D. Goodhue; P. E. Tannenwald; C. D. Parker; D. D. Peck. Resonant tunneling through quantum wells at frequencies up to 2.5 THZ. *Appl. Phys. Lett. 43, 588*, 1983.

[16] F. Capasso. *Physics of Quantum Electron Devices*. Heidelberg, Springer Verlag, 1990.

[17] L. L. Chang; E. E. Mendez; C. Tejedor. *Resonant Tunneling in Semiconductors: Physics and Applications*. New York, Plenum Press, 1991.

[18] IOFFE Institute. Physical Properties of Semiconductors. Website : "http://www.ioffe.ru/SVA/NSM/", 1998-2001. last accessed on 05.03.2011.

[19] P. Bhattacharya. *Properties of Lattice-Matched and Strained Indium Gallium Arsenid*. London: INSPEC the Institute of Electrical Engineers, 1993.

[20] M. Levinshtein; S. Rumyantsev; M.Shur. *Handbook Series on Semicconductor Parameters Volume 2*. Singapore, World Scientific Publishing Co., 1996.

[21] H. Liu; O. Ostinelli; Y. Zeng; C. R. Bolognesi. High-performance InP/GaAsSb/InP DHBTs grown by MOCVD on 100mm InP substrates using PH3 and AsH3. *IEEE Trans. Electron Devices 54 (2007) 27922795*, 2007.

[22] U. Seidel; H.-J. Schimper; Z. Kollonitsch; K. Schwarzburg; T. Hannappel. Growth of an InGaAs/GaAsSb tunnel junction for an InP-based low bandgap tandem solar cell. *J. Crystal Growth 298 (2007) 777781*, 2007.

[23] M. Levinshtein; S. Rumyantsev; M. Shur. *Handbook Series on Semicconductor Parameters Volume 1*. Singapore, World Scientific Publishing Co., 1996.

[24] J. Hu; X. G. Xu; J. A. H. Stotz; S. P. Watkins; A. E. Curzon; M. L. W. Thewald; N. Matine; C. R. Bolognesi. Type II photoluminescence and conduction band offsets of GaAsSb/InGaAs and GaAsSb/InP heterostructures grown by metalorganic vapor phase epitaxy. *Appl. Phys. Lett. 73, 2799*, 1998.

[25] P. Devlin; H. M. Heravi; J. C. Wooley. Electron effective mass values in GaAsxSb1-x alloys. *Canadian Journal of Physics 59:939-944, 10.1139/p81-123*, 1981.

[26] I. Vurgaftman; J. R. Meyer; L. R. Ram-Mohan. Band parameters for III-V compound semiconductors and their alloys. *J. Appl. Phys. 89, 5815*, 2001.

[27] E. Benveniste; A. Vasanelli; A. Delteil; J. Devenson; R. Teissier; A. Baranov; A. M. Andrews; G. Strasser; I. Sagnes; C. Sirtori. Influence of the material parameters on quantum cascade devices. *Appl. Phys. Lett. 93, 131108*, 2008.

[28] M. J. Kelly. *Low-Dimensional Semiconductors Materials, Physics, Technolgy, Devices*. Oxford: Clarendon Press, 1995.

[29] P. R. Holland. *The Quantum Theory of Motion: An Account of the de Broglie-Bohm Causal Interpretation of Quantum Mechanics*. Cambridge University Press, 1995.

[30] Martin Bäker; Science Blogs. Die Schrödingergleichung - Teil VII: Mit dem Kopf durch die Wand. Website : "http://www.scienceblogs.de/hier-wohnen-drachen/2010/11/die-schrodingergleichung-teil-vii-im-tunnel.php", 2008. last accessed on 05.03.2011.

[31] L. S. Sheng. *Semiconductor Physical Electronics*. New York, Plenum Press, 1993.

[32] R. Tsu; L. Esaki. Tunneling in a finite supperlattice. *Appl. Phys. Lett. 22, 562*, 1973.

[33] S. Datta. *Electronic Transport in Mesoscopic Systems*. Cambridge: Cambrigde University Press, 1995.

[34] N. C. Kluksdahl; A. M. Kriamn; D. K. Ferry; C. Ringhofer. Self-consistent study of resonant-tunneling diode. *Phys. Rev. B, 39(11):77207735*, 1989.

[35] F. Chevoir; B. Vinter. Scattering-assisted tunneling in double barrier diodes: Scattering rates and valey current. *Appl. Phys. Lett., 24(12):5935*, 1993.

[36] Andrew R. Barron. Molecular Beam Epitaxy. Website : "http://cnx.org/content/m25712/latest/", 2009. last accessed on 05.03.2011.

[37] G. Strasser. *Prozesstechnologien der Mikroelektronik*. Technical University Vienna, LVA Nr. : 362.085, 2005.

[38] H. Lüth. *Solid Surfaces, Interfaces and Thin Films*. Springer, 2001.

[39] E. Bertagnolli. *Integrierte Bauelemente*. Technical University Vienna, LVA Nr. : 362.088, 2005.

[40] Semipark. Fig.10 Action Chamber. Website : "http://www.semipark.co.kr/semidoc/basic/plasma.asp", 2000. last accessed on 05.03.2011.

[41] I. Brodie; J. J. Muary. *The Physics of Micro/Nano-Fabrication*. New York, Plenum Press, 1992.

[42] C. Dupas; P. Houdy; M. Lahmani. *Nanoscience*. Heidelberg: Springer Verlag, 2006.

[43] MEMSnet. Etching Processes; Figure 2: Typical parallel-plate reactive ion etching system. Website : "http://www.memsnet.org/mems/processes/etch.html". last accessed on 05.03.2011.

[44] C. Schwarzer. Coherent coupling of ring cavity intersubband lasers. Master's thesis, Vienna University of Technology, 2010.

[45] H. Geng. *Semiconductor manufacturing handbook*. United States of America: The Mac-Graw Hills Company, 2006.

[46] E. Mujagic. Impact of doping density in short-wavelength indium phosphide quantum cascade lasers. Master's thesis, Vienna University of Technology, 2007.

[47] J. J.Vossen; W. Kern. *Thin film processes II*. San Diego: Academic Press INC., 1991.

[48] Gary E. McGuire; University of Florida. Development of liftoff processes for patterning of magnetic and other materials. Website : "http://www.phys.ufl.edu/~nanoscale/reports/year1/liftoff.html". last accessed on 05.03.2011.

[49] S. A. Dyer. *Survey of instrumentation and measurement*. Wiley-IEEE Press, 2001.

[50] A. Bergauer; C. Eisenmenger-Sittner. *Physik und Technologie Dünner Schichten*. Vienna University of Technology.

[51] S. Golka. *Dry-etched intersubband devices for near- and mid-infrared optoelectronics*. PhD thesis, Vienna University of Technology, 2006.

[52] Gregory Snider. 1D Poission. Website : "http://www.nd.edu/~gsnider/". last accessed on 05.03.2011.

[53] Michael Schwantzer and Hermann Detz. to be published.

[54] J. S. de Sousa; H. Detz; P. Klang; M. Nobile; A. M. Andrews; W. Schrenk; E. Gornik; G. Strasser; J. Smoliner. Nonparabolicity effects in InGaAs/GaAsSb double barrier resonant tunneling diodes. *Journal of Applied Physics 108, 073707*, 2010.

[55] Courtesy of Silvano de Sousa; Jürgen Smoliner *et al.*

Acknowledgements

This thesis can not be considered finished without mentioning all the people who helped me finalizing this work as well as made it possible for me to complete my studies at the Vienna University of Technology. First of all, I want to give my sincere thanks to Prof. Gottfried Strasser, who made it possible to end my studies with such an interesting topic and had always the time to help. Furthermore, without the extensive knowledge about growth, fabrication and theory and most important, the never-ending support from Hermann Detz, this thesis would have not been possible. For that and his invested time to proof-read this thesis, he has my greatest thanks. Additionally, I want to thank all my colleagues for the important discussions and ideas which helped to finish this work, especially Elvis Mujagic, from who I always got important inputs and ideas about fabrication and theory as well as Werner Schrenk, who can be best described as a walking lexicon, J. Silvano de Sousa for his extended knowledge about RTDs and his will to discuss this topic with me endless times and Michele Nobile for his extensive support. Not to forget, Aaron Maxwell Andrews, Pavel Klang, Stefan Kalchmair, Sangil Ahn, Clemens Ostermaier, Bernhard Basnar, Clemens Schwarzer, Alexander Alexcewics, Roman Gansch, Tobias Zederbauer and Alexander Pfnier for their help to create a working environment, where finishing this thesis and my studies was a pleasure due to the high technical and scientific competence of this group as well as for the hours of laughter and fun to clear my mind and made it possible to recharge my energy to finish this thesis.

Last but not least, my deepest gratitude goes to my parents Peter and Christine Schwantzer for their endless support and trust as well as to my fiancée Barbara Weber, who never stopped believing in me and always motivated me to go on. Without you, I would not be writing this today. For this and the fact that you are always there for me, you have my never-ending gratitude.